Theses and Dissertations

6-30-2016

Comparative Analysis Of Current Control Methods For Modular Multilevel Converters

Jordan D. Rogers
University of South Carolina

COMPARATIVE ANALYSIS OF CURRENT CONTROL METHODS FOR MODULAR
MULTILEVEL CONVERTERS

by

Jordan D. Rogers

Bachelor of Science
University of South Carolina, 2013

_____

Submitted in Partial Fulfillment of the Requirements

For the Degree of Master of Science in

Electrical Engineering

College of Engineering and Computing

University of South Carolina

2016

Accepted by:

Herbert Ginn III, Director of Thesis

Andrea Benigni, Reader

Lacy Ford, Senior Vice Provost and Dean of Graduate Studies

ABSTRACT

Modular Multilevel Converters (MMCs) are power electronic converters comprised of a series connection of sub-modules. Their modular structure allows for the possibility to design high-voltage converters that are suitable for utility applications due to the modular fail-safe structure with reduced switching frequency requirements. Some areas of interesting research specific to the MMC topology include modulation techniques, control methods, capacitor voltage balancing strategies, and circulating current suppression control. This thesis presents the development of a predictive current control for MMCs that has the benefit of inherently reduced circulating currents within the converter's phase units. Two other typical MMC current control strategies are implemented for comparison with the predictive current control.

The operation and modeling, multi-loop control design, and digital simulation of a MMC are presented using MATLAB/Simulink software. An effective control scheme is implemented using a cascade control approach, with an outer power controller and an inner current controller. The outer loop is implemented with a conventional synchronous proportional-integral (PI) controller. The inner loop is then implemented with PI, proportional resonant (PR), and predictive controllers and the controller error signal dynamics for each method are observed. The predictive arm-current controller is shown to have significantly reduced circulating currents in the phase units, which reduces arm current distortion and submodule capacitor voltage ripple.

TABLE OF CONTENTS

LIST OF TABLES

LIST OF FIGURES

LIST OF ABBREVIATIONS

HVDC .... High voltage direct current

IGBT ....Insulated-gate Bipolar Transistor

MMC.. Modular Multilevel Converter

PD-PWM...Phase-disposition Pulse-width Modulation

PI... Proportional Integral

PR..Proportional Resonant

PSC-PWM..Phase-shifted Carrier Pulse-width Modulation

SVM... Space Vector Modulation

VSC.. Voltage-source Converter

CHAPTER 1

MODULAR MULTILEVEL CONVERTERS

1.1 INTRODUCTION

The modular multilevel converter (MMC) was first proposed for high voltage applications by Dr. Lescinar in [1]. The MMC is a three-phase converter composed of low voltage semiconductor valves that can be manipulated to behave like controlled voltage sources in medium and high voltage applications. The MMC is a scalable technology with many advantages over more conventional two and three level voltage source converters (VSCs). Its modular topology allows for scalability of medium to high voltage ranges, as well as for control of harmonic distortion by varying the number of submodules used in the design. This converter topology also allows for lower switching frequency requirements, which significantly decreases the converter's switching losses. Modular multilevel converters are also suitable for use in interfacing renewable energy power sources to the conventional AC grid.

This thesis will focus on the MMC topology described below and will specifically investigate three different digital current control techniques. The different approaches for digital current control have a significant effect on the converter's operation such as its transient response, capacitor voltage ripple, circulating current magnitude, and harmonic distortion of the output waveforms. Specifically, this thesis investigates two conventional strategies and a third novel approach and demonstrates the advantage of inherent

circulating current suppression with the third strategy. The techniques used in the design of each of the controllers are described in detail, and then the implementations and simulated results follow.

1.2 MMC TOPOLOGY

The converter is composed of six arms, two per phase, that are each connected to one AC terminal and one DC terminal. The structure of each arm is composed of N series-connected submodules and a current limiting inductor, L_o, as shown in Figure 1.1.

N sub-modules

SM1

SM2

SMN

arm

L_o
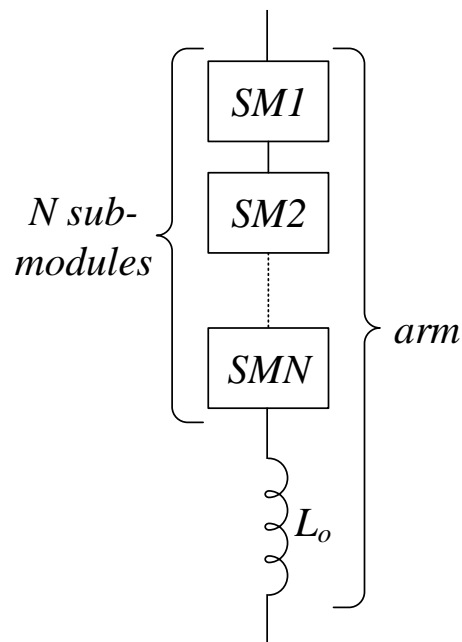
Figure 1.1 Modular multilevel converter arm

Each phase leg of the converter, or phase unit, is composed of an upper and a lower arm. Each phase unit is attached to the AC terminal between the two arm inductors and to the DC terminals at the opposite ends of the arms. The structure of a three-phase MMC is shown in Figure 1.2.
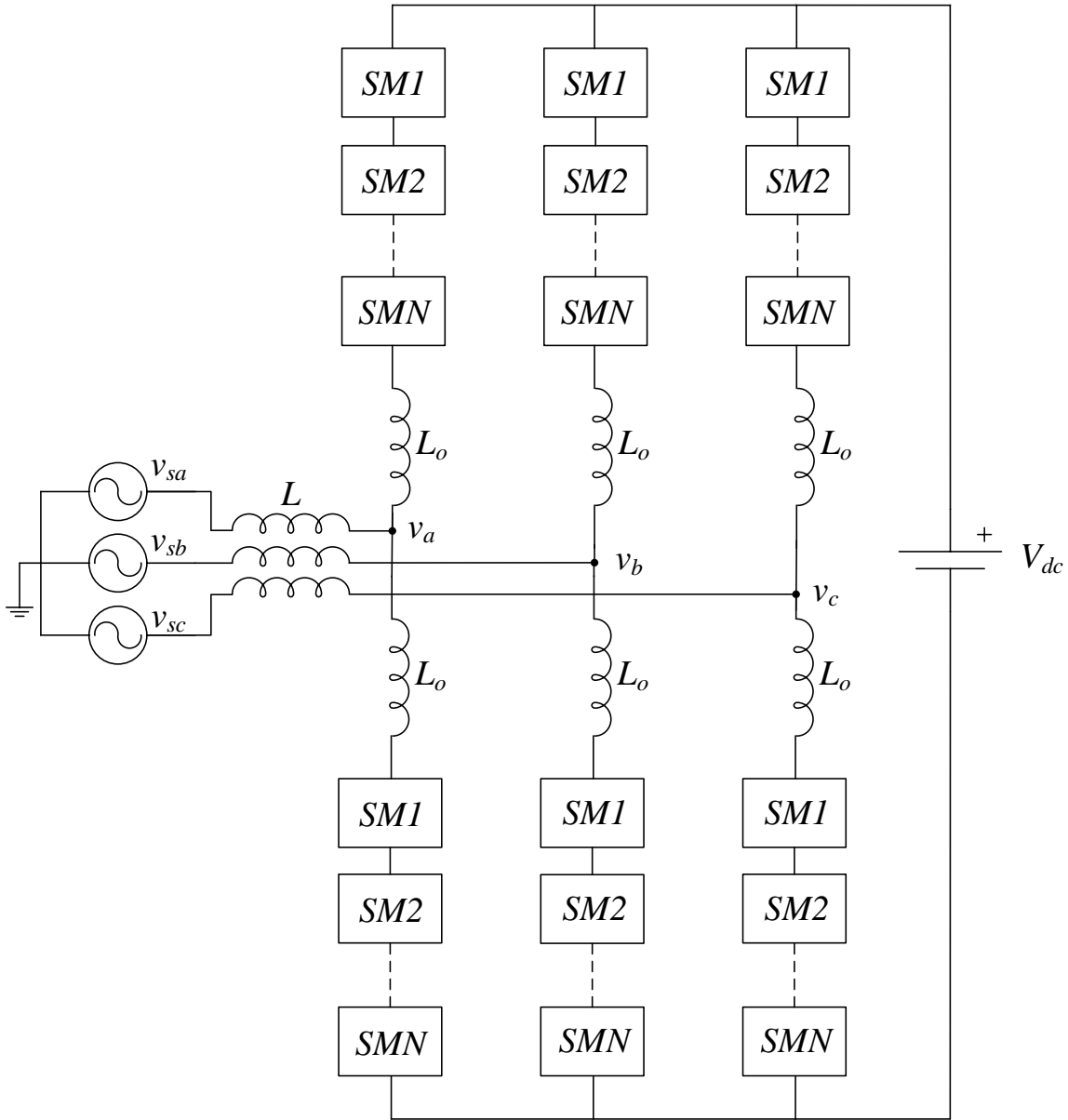
Figure 1.2 Modular multilevel converter topology

Each submodule consists of two controllable semiconductor switches and a storage capacitor, C_o. In this case, the switches are insulated-gate bipolar transistors (IGBTs). The submodule structure is shown in Figure 1.3 and the two switches are complimentary, such that C_o is either connected in the arm or bypassed.
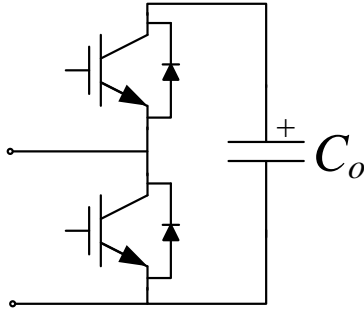
Figure 1.3 MMC Submodule

While the upper switch is conducting and the lower is not, the capacitor is inserted into the arm with a nominal voltage V_{dc}/N. Then, while the lower switch is conducting and the upper is not, the storage capacitor is bypassed. The freewheeling diodes allow for reverse current flow when the current through the submodule is negative.

Each arm voltage is controlled by inserting and bypassing the appropriate number of submodules to produce the desired voltage waveform at the terminals. The control of each submodule's conduction state allows for the total arm voltage to be controlled independently to $N+1$ discrete voltage levels. Zero volts is included as a level; thus, the MMC naming convention is that of an $(N+1)$-level converter. If a higher number of submodules is used, a higher quality voltage waveform can be produced because of the ability to adjust the output by smaller voltage increments; however, the increase of submodules adds control complexity, increased computational power requirements, and higher switching device losses. The most significant driving factor for selecting the appropriate level of an MMC is the voltage level required in the application for which it will be utilized.

1.3 PRINCIPLE OF OPERATION

The three-phase equivalent circuit of an idealized MMC is shown in Figure 1.4, where the submodules in each converter arm are represented by a controlled voltage source. Each of the DC busses are connected to each end of two series-connected DC sources denoted V_{dc}^+ and V_{dc}^-.
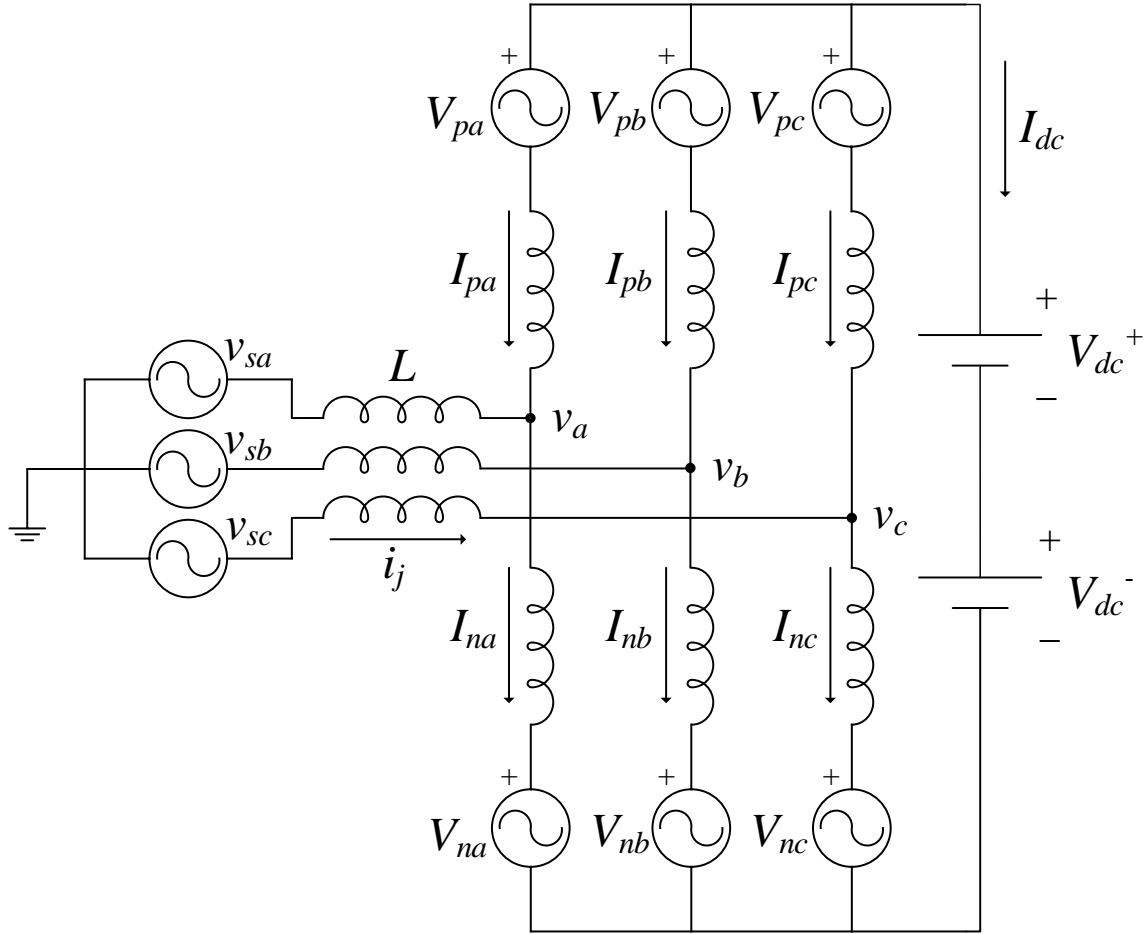
Figure 1.4 Three-phase MMC equivalent circuit

V_{dc}^+ and V_{dc}^- can be approximated by (1), where V_{dc} is the total DC bus voltage. The line inductors, L, are considered to be very small, such that $v_{sa} \approx v_a$. By applying KVL to the equivalent circuit, the equations for the arm voltages can be shown by (2) and (3). V_{pj} and V_{nj} denote the arm voltages, where j denotes the phase a, b, or c and p and n

represent the positive and negative arm in the phase unit, respectively. Making the assumption that the arm inductor value is very small, which is often true, the arm inductor's voltage can be ignored. Substituting (2) into (3), (4) can be obtained.

$$V_{dc}^+ = V_{dc}^- = \frac{V_{dc}}{2} \qquad (1)$$

$$V_{pj} = \frac{V_{dc}}{2} - v_j \qquad (2)$$

$$V_{nj} = \frac{V_{dc}}{2} + v_j \qquad (3)$$

$$v_j = \frac{(V_{nj} - V_{pj})}{2} \qquad (4)$$

The phase currents and arm currents can be defined by (5)-(7), and the circulating current for each phase, i_{cirj}, by (8), where j denotes phase a, b, or c.

$$i_j = I_{nj} - I_{pj} \qquad (5)$$

$$I_{pj} = i_{cirj} + \frac{i_j}{2} \qquad (6)$$

$$I_{nj} = i_{cirj} - \frac{i_j}{2} \qquad (7)$$

$$i_{cirj} = \frac{(I_{pj} + I_{nj})}{2} \qquad (8)$$

It is important to note that the description of the different operational sections of an MMC will vary between "upper and lower" and "positive and negative." It should be clarified that the descriptions of "upper" and "positive" refer to the same section of the converter, which contains the arms connected to the positive side of the DC bus, V_{dc}^+. Similarly, "lower" and "negative" both describe the arms connected to the negative side of the DC bus, V_{dc}^-.

6

The circulating current, i_{cirj}, is a continuously flowing current present in all six arms that is responsible for the power transmission of the converter, and does not affect the AC-side voltages and currents. The undesirable circulating currents in an MMC are due to voltage differences between each of the phase units, and are superimposed onto the DC current flowing through each of the phase units [2]-[4]. The DC component in each arm is quantified by the division of the total DC current by the number of phase units. The AC components oscillate with twice the fundamental frequency and are negative-sequence [21]. The equation for the total circulating current is defined by (9).

$$i_{cirj} = \frac{I_{dc}}{3} + i_{2fj} \qquad (9)$$

Here, i_{cirj} is the circulating current in each phase, I_{dc} is the total DC current present in the converter, and i_{2fj} is the unwanted AC current circulating between the phase units at twice the fundamental frequency.

1.4 MODULATION TECHNIQUES

The number of submodules required to be on or off in each of the converter's arms is driven by the modulation scheme. The modulator enforces the desired state of the complementary gates in each of the submodules, resulting in the average arm voltage needed for that time step. Pulse-width modulation (PWM) techniques are commonly used in power electronic converters to achieve frequency and voltage variability. There are a variety of techniques that can be used in the creation of PWM control signals, which can allow for the reduction of harmonic distortion in the output waveforms and increased modulation indexes, depending on the application.

Conventional pulse-width modulation uses one carrier waveform and one reference waveform to generate a gate-driving signal. The carrier is some cyclical waveform, typically either sawtooth or triangular, that is used as a comparison to the reference. For example, when the reference is higher than the carrier, the PWM output is high and when the reference becomes lower than the carrier, the PWM output transitions to a low state. Of course, this convention can easily be reversed. Figure 1.5 shows a single update sinusoidal reference PWM example, where Pulse 1 and Pulse 2 demonstrate the two conventions and the so-called reference signal is labeled as "Internal generation signal."
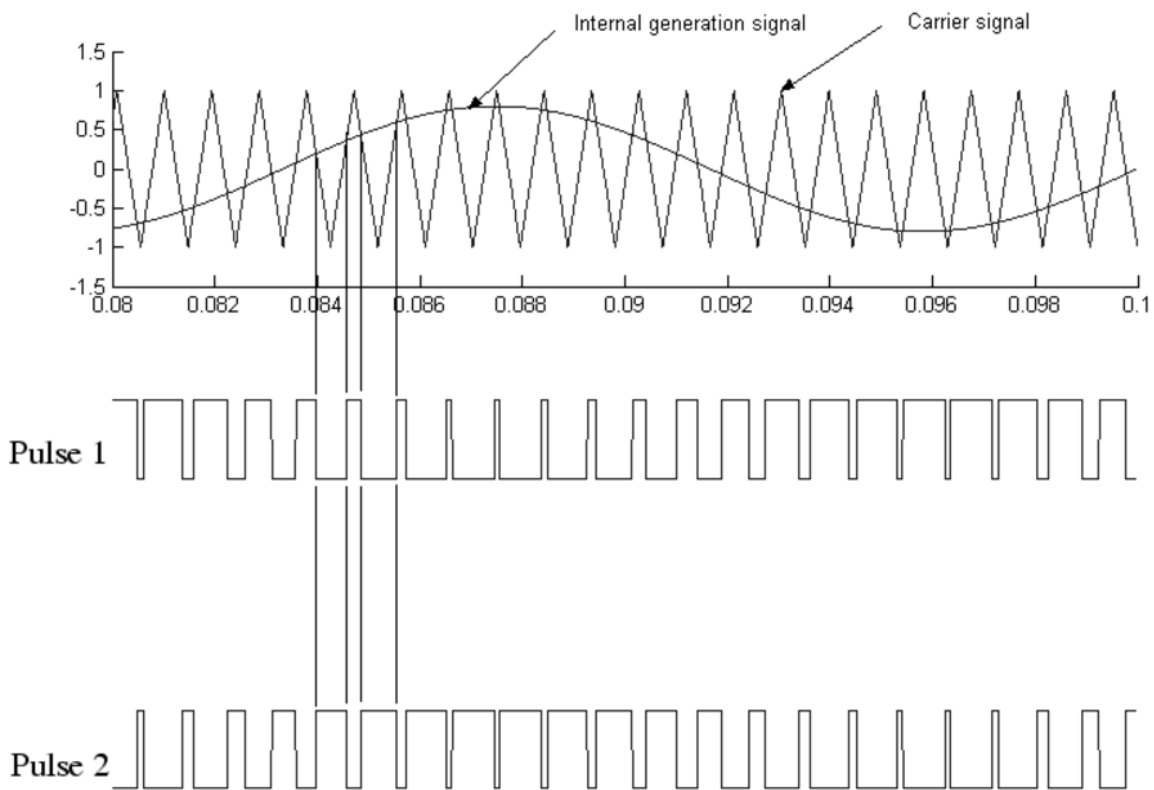
Figure 1.5 Sinusoidal PWM generation [5]

This configuration is suitable for the control of a half-bridge circuit of a single phase inverter. Pulses 1 and 2 would control the states of each upper and lower switch.

In multilevel converters, there are many of these half-bridge circuits that need to be controlled independently. The solution to this is to use a multicarrier PWM method. References [6] and [13] investigate different PWM methods for MMCs. When these multicarrier modulation techniques are applied in an MMC, there is one carrier wave for each of the submodules. For the phase-shifted carrier pulse width modulation (PSC-PWM) method, triangular carriers are typically used and each of the carriers has an equal phase shift between them. The required phase difference calculation is shown in (10), where N is the number of submodules in one arm and θ is the phase shift between each carrier waveform.

$$\theta = \frac{360°}{N} \tag{10}$$

By increasing the number of carrier waves, the effective switching frequency of the converter is also increased by a factor of N, shown in (11), where f_s is the converter's switching frequency and f_c is the carrier frequency.

$$f_s = f_c \times N \tag{11}$$

Figure 1.6 shows an example of a 20 triangular carrier implementation of PSC-PWM. The sinusoidal trace represents the reference signal and the phase shift between carriers is 18°. The carrier frequency is 60 Hz; so, for an MMC with 20 submodules per arm, this example has an effective switching frequency of 1.2 kHz.
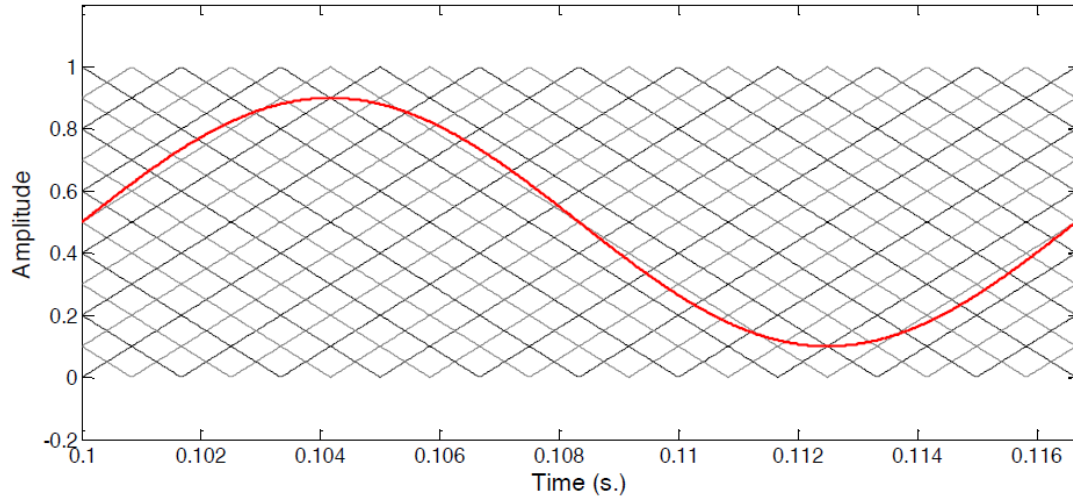
Figure 1.6 20 submodule PSC-PWM [6]

It is interesting to show that the resulting PWM waveforms produced to drive the state of each submodule in an arm can be summed to create a single waveform. This waveform, shown in Figure 1.7, represents the total number of submodules required to be connected in the arm to achieve the desired voltage level at each time step. For clarity, six cycles are shown in this plot.
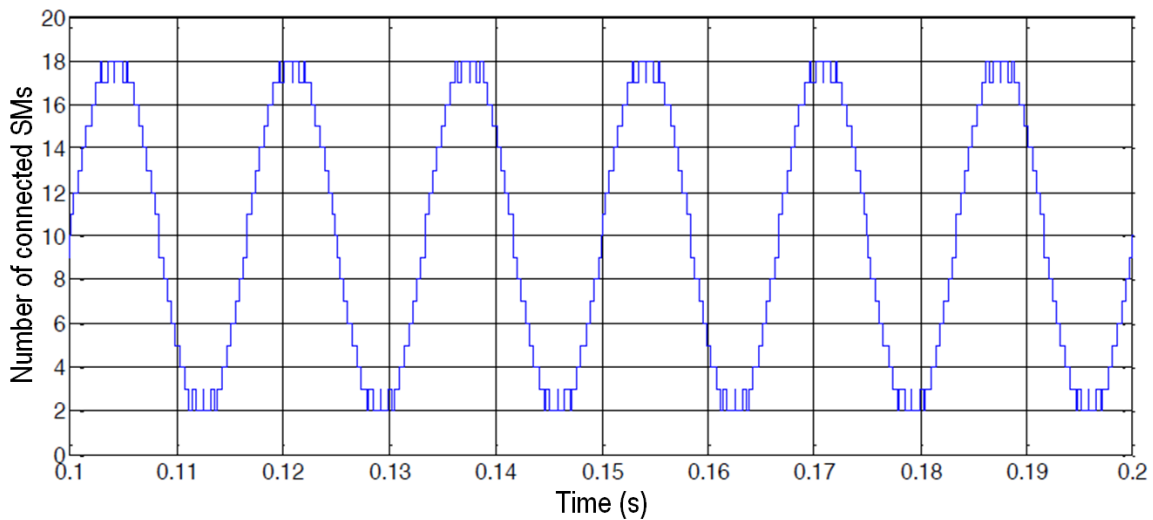
Figure 1.7 PSC-PWM Reference waveform for 21-level MMC [6]

PSC-PWM is used as the modulation technique for this study. References [6] and [7] provide an analysis of alternative PWM methods such as phase-disposition PWM (PD-PWM) and space-vector modulation (SVM) for multilevel converters. PSC-PWM is chosen because of its inherent reduction of capacitor voltage ripple and minimization of converter power loss, as explained in [6].

1.5 CAPACITOR VOLTAGE BALANCING

Another important concept to understand about MMCs is the necessity of voltage balancing of the submodule capacitors. Similar to other multilevel topologies, the submodules in an MMC have storage capacitors that are switched into and out of the circuit that must be monitored in order to regulate each one's voltage ripple. While the current direction in the arm is positive, the capacitors connected during that time step will be charging, and when the current direction in the arm becomes negative, the capacitors connected during that time step will be discharging. This action causes voltage imbalances between some of the capacitors in the arm, which creates unwanted circulating currents.

In order to minimize the imbalance, all of the submodule capacitors are monitored and sorted based on their voltage levels during a particular control cycle. An intuitive algorithm to implement this balancing technique is displayed in Figure 1.8. This algorithm will be implemented for all simulations presented in this study.
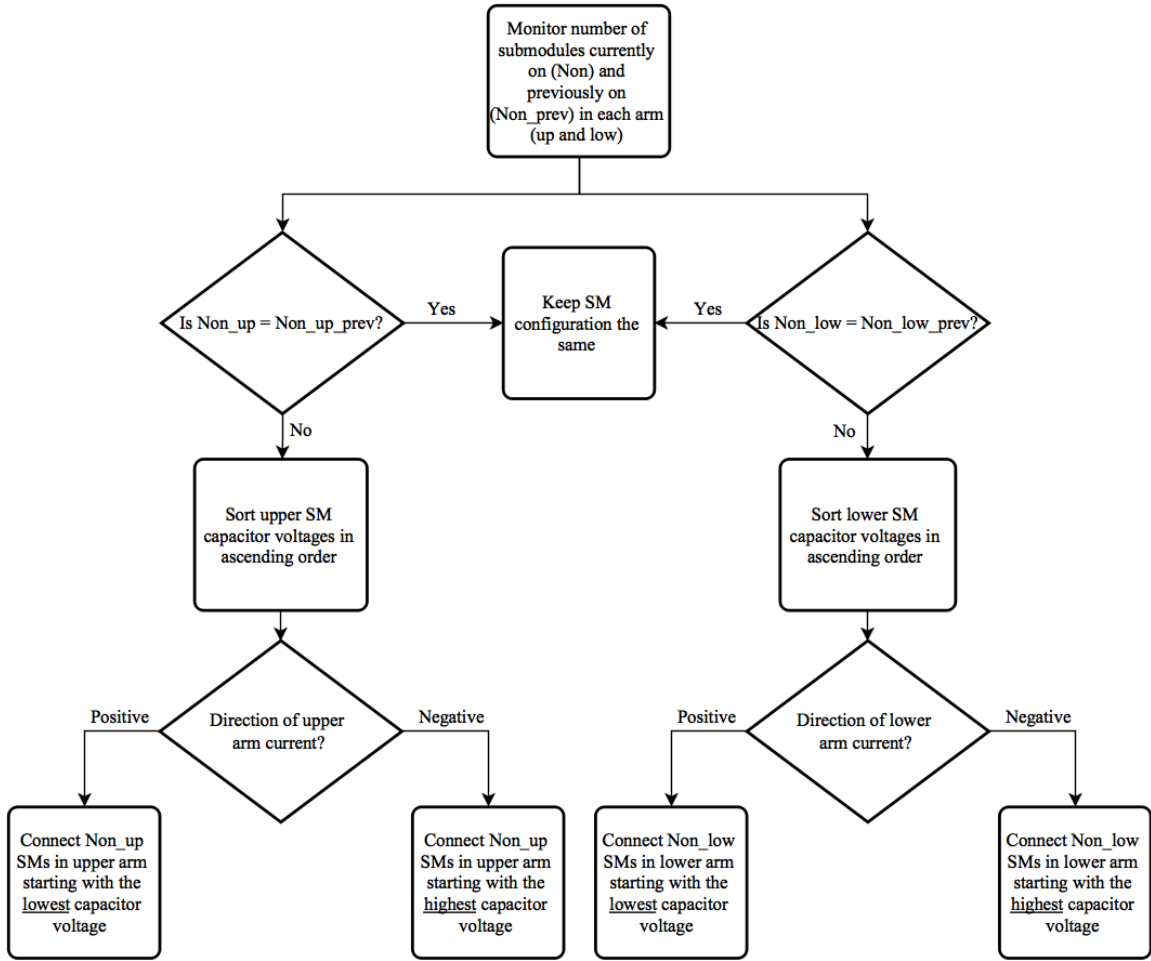
Figure 1.8 Capacitor voltage balance algorithm

When a submodule has its capacitor connected to the circuit, it will be considered "on"; while a submodule has its capacitor shorted out in the circuit, it will be considered "off". This algorithm is inserted in the system for each of the three phases, so the upper and lower arms of each phase unit are denoted with "up" or "low" to indicate the upper or lower arm.

While the fundamental principle of voltage balancing algorithms are the same, the difference for this application arises in how many submodule states are changed due to capacitor voltage imbalance during each control cycle because that directly affects the

converter's effective switching frequency. The compromise is generally between effective switching frequency and maximum capacitor voltage ripple. The main benefit of reducing the ripple is the reduction in the capacitor size, thus decreasing the cost and weight of the MMC. The acceptable capacitor voltage ripple range is typically $\pm$5-10% [6]. There are various ways to perform capacitor voltage balancing for an MMC such as the methods investigated in [8] and [9].

CONTROL STRATEGIES AND TUNING

The control strategy for a grid-connected MMC consists of a digital current mode control scheme, which is identical to the conventional vector control used in a two-level VSC [10]. The term used for this type of control is cascade control, which means there are two interconnected control loops: a primary loop and a secondary loop. The primary loop, otherwise called the outer loop, controls the active and reactive power and regulates the converter's output voltage. The secondary loop, otherwise called the inner loop, is a feedback loop inserted into the primary loop that directly controls the inductor current of the converter. The primary active and reactive power (PQ) controller generates the set point for the inner current controller. A generalized block diagram of the control loop is shown in Figure 2.1.
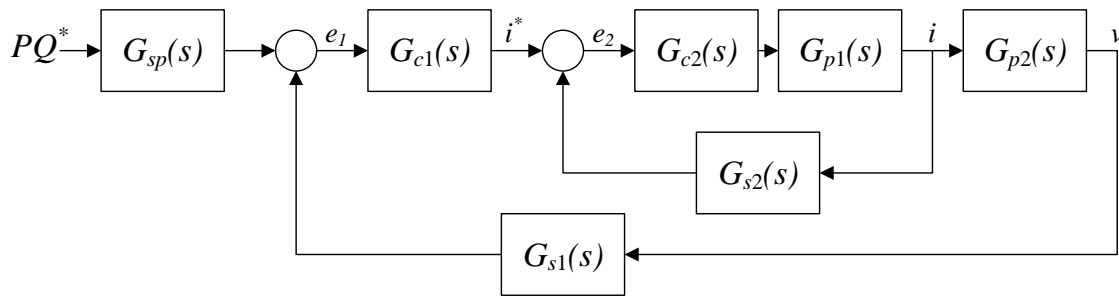
Figure 2.1 Current mode control loop

In the figure, G_{c1} and G_{c2} are the respective primary and secondary controllers, G_{p1} and G_{p2} are the controlled processes, and G_{s1} and G_{s2} are sensor gains.

In addition, there is a capacitor voltage balancing mechanism and typically a circulating current suppression controller. For the purpose of this study, independent circulating current suppression control will not be implemented so that the inherent suppression performance contributed by the proposed control strategy can be appropriately compared to the other standard control strategies.

This chapter will introduce the two parts of the cascaded control loop for an MMC and go through the design process for each. The inner current control loop methods to be implemented are proportional-integral (PI), proportional-resonant (PR), and predictive, or digital deadbeat, control. The general tuning strategy to be used is based on the damping ratio of the closed-loop systems. The inner loop will be designed independently, where the system's associated damping ratio can be extracted. In an attempt to make an accurate comparison, each current controller will be tuned to have a so-called technical optimum damping ratio. In the case of the predictive control method, however, there are no user defined coefficients that directly affect the damping ratio. This controller will be optimally tuned, which is explained in a later section.

The outer loop will be one of voltage control. The controlled output voltage along with the converter output current will be measured and multiplied in order to create an instantaneous power measurement ($P(t)$ and $Q(t)$). The control diagram shown in Figure 2.2 includes PQ control, current control, and the modulation and voltage balancing. $G_{PC}(s)$ and $G_{CC}(s)$ are the power regulator and current controller transfer functions, respectively. The power regulator $G_{PC}(s)$ will be implemented by a synchronous PI controller for all simulations.
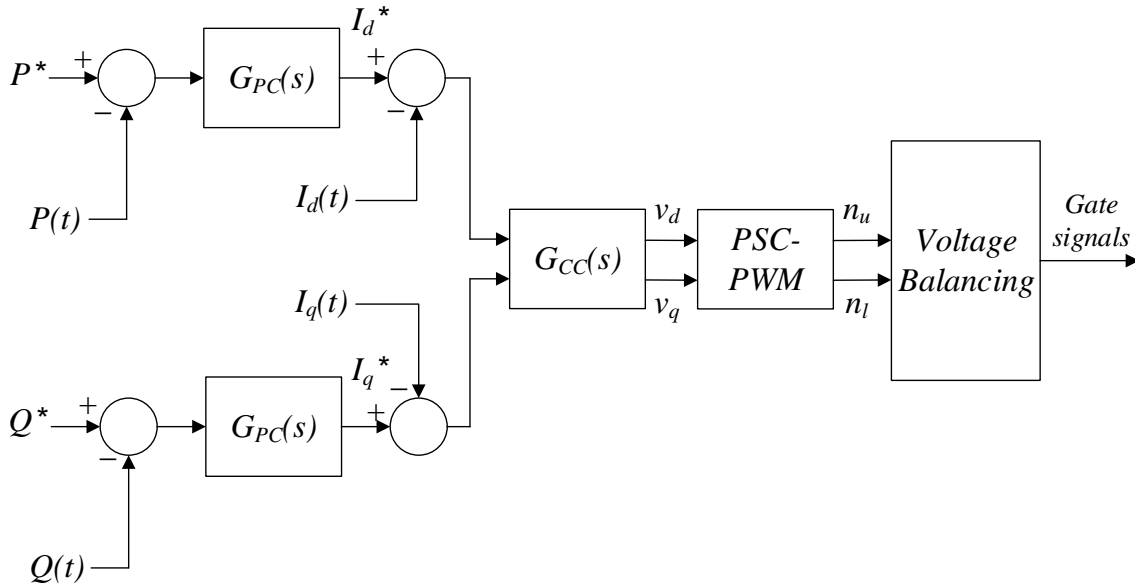
Figure 2.2 MMC control diagram

2.1 BACKGROUND

The analytical design of the controllers begins with the transfer function of the system it is tasked with controlling. The inner loop is to command the controlled voltage sources in each arm in order to achieve a desired inductor current for each phase. This means there should be either be a dedicated current controller for each phase, or some method to relate the three phase currents and then directly control that relation. Since the arm voltage is controlled directly to achieve the desirable arm current, the dc-coupling term can be ignored and each phase of the converter can be represented by the equivalent circuit shown in Figure 2.3. R_o and L_o are the arm inductance and that inductor's series resistance value, which is typically very small.
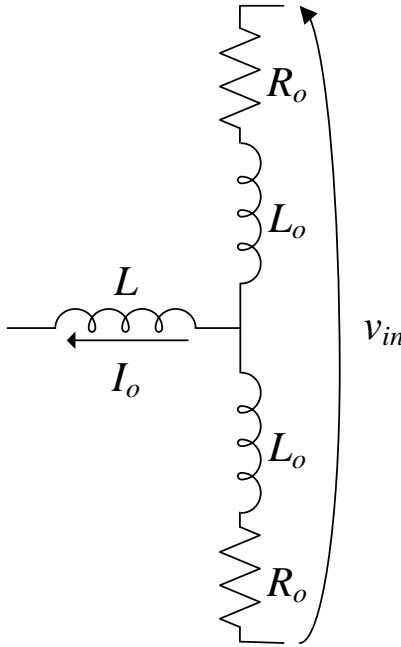
Figure 2.3 Phase leg equivalent circuit

From the equivalent circuit, the transfer function for an MMC can be defined in (12).

$$G_{MMC}(s) = \frac{i_o(s)}{v_{in}(s)} = \frac{1}{sL_o + R_o} \tag{12}$$

2.1.1 PARK'S TRANSFORMATION

The current controller for all three implementations needs to be able to regulate current according to a sinusoidal reference. In order to implement a standard PI controller on this kind of system, a coordinate transformation such as the Park transform must be performed. This is because a PI controller has a finite closed-loop gain at a particular frequency of interest, which causes a non-negligible tracking error when applying an oscillatory reference such as a sinusoidal one. In general, electrical systems can be mathematically described using a set of dynamic equations; however, in the case of three-phase power systems, the three models are not independent of each other. This relationship allows the model to be reduced to a simplified set of dependent equations

without the loss of any information [10]. The first step is possible by the so-called alpha-beta ($\alpha\beta$), or Clarke transformation. This transformation simplifies a three-dimensional system model into a two-dimensional system model by using the linear transformation shown in (13).

$$\begin{bmatrix} x_\alpha \\ x_\beta \\ x_\gamma \end{bmatrix} = \frac{2}{3} \begin{bmatrix} 1 & -1/2 & -1/2 \\ 0 & \sqrt{3}/2 & -\sqrt{3}/2 \\ 1/2 & 1/2 & 1/2 \end{bmatrix} \begin{bmatrix} x_a \\ x_b \\ x_c \end{bmatrix} \tag{13}$$

This transformation can be simplified when assuming a balanced system by setting the x_γ term equal to zero. The effect of this transformation can be effectively visualized as a vector $\overrightarrow{x_{\alpha\beta}}$ rotating along a two-dimensional $\alpha\beta$ reference frame at an angular frequency ω. When the transformation is applied to three symmetrical and balanced sinusoidal signals, like in the case of a three-phase power distribution system, the resultant is two sinusoidal signals with a $90°$ phase shift and oscillating at the distribution system's fundamental frequency.

For the purpose of the aforementioned PI controller application, the reference signal applied should be of constant value in order to optimize the controller's operational benefit of achieving zero steady-state error. To do this, the Park transformation can be used. Park's transformation defines a new set of axes, d and q, that rotate around the $\alpha\beta$ reference frame at a constant angular frequency. It can be visualized that if the dq axes are rotating at the same angular frequency, ω, of the vector $\overrightarrow{x_{\alpha\beta}}$, then the previously generated sinusoidal signals will be seen as two constant signals in the new dq reference frame. The transformation matrix is shown below in (14).

$$\begin{bmatrix} x_d \\ x_q \end{bmatrix} = \begin{bmatrix} \cos(\omega t) & \sin(\omega t) \\ -\sin(\omega t) & \cos(\omega t) \end{bmatrix} \begin{bmatrix} x_\alpha \\ x_\beta \end{bmatrix} \tag{14}$$

These constant *dq* frame quantities can now be used as reference signals for a conventional PI controller, as long as the feedback measurement is also converted to the *dq* frame before the loop is closed.

2.1.2 POWER REGULATOR DESIGN

The outer control loop of the converter is PQ regulator that generates a current reference signal for the inner current controller based on the system's instantaneous power measurement. A simple block diagram of the power regulator is shown in Figure 2.4.
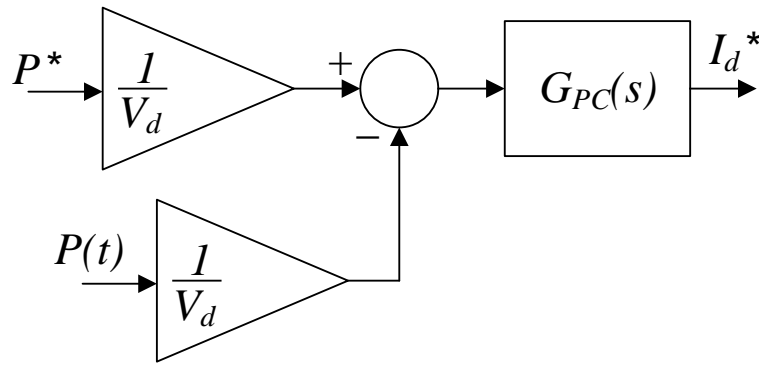
Figure 2.4 Power regulator block diagram

In the figure, *P(t)* is the measured instantaneous active power, *P** is the reference power set to be delivered by the converter, V_d is the AC-side voltage measurement in the *dq* frame, which is constant for a balanced system, and I_d* is the reference current generated by the controller, $G_{PC}(s)$.

It should be noted that in this study the reactive power reference signal Q^* will be assumed to be zero. Although reactive power control is possible with an MMC, its implementation and results are outside the scope of this study.

The controller to be used for power regulation is a conventional dq-frame PI controller. The general form of the PI controller transfer function used as the power regulator $G_{PC}(s)$ is defined in (15),

$$G_{PC}(s) = \frac{I_d^*(s)}{e_P(s)} = \frac{sk_p + k_i}{s} \tag{15}$$

where $e_P(s)$ is the error between the power reference and the measured instantaneous power. The closed-loop control design and stability analysis is performed in the continuous-time domain and then transformed into the discrete-time domain. This approach is acceptable assuming the system's sampling time is small enough.

When designing a multi-loop control system like this one, it is important to consider the effects the inner loop will have on the outer loop. It is demonstrated in [11] that in order to determine the loop gain for the outer primary loop, one must first establish the stability and closed-loop properties of the inner secondary loop. The minor loop is then simply incorporated as a gain in the primary loop. With this in mind, the generalized control loop can be simplified as Figure 2.5 for the power regulator design.
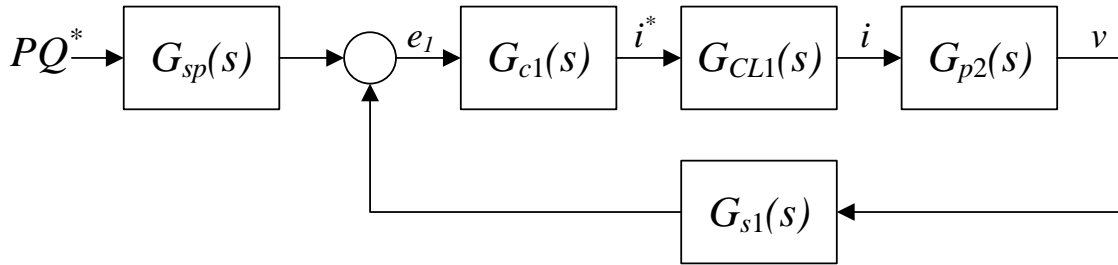

Figure 2.5 Simplified primary control loop

$G_{CL1}(s)$ is the closed-loop transfer function of the secondary current loop control system.

The inner loop generally has a much faster response than the outer loop, which means the crossover frequency for the inner loop is much higher than the bandwidth for

the outer loop. The outer voltage loop will be designed to have a bandwidth equal to that of the fundamental frequency of the MMC system, which is 60 Hz. In an ideal case, the two bandwidth limits would be far enough apart in the frequency domain that the two loop gains would not operationally affect each other. If that were the case, then $G_{CL1}(s)$ could be simplified to a gain of 1. In an actual implementation, however, there is a limit to the upper bounds of the inner loop's bandwidth; a general rule is to design the inner loop to be at least ten times faster than the outer loop. In any case, it is usually acceptable to approximate the inner loop gain $G_{CL}(s)$ as a real pole located at its designated cutoff frequency. This approximation imitates the attenuation and phase shift around the inner loop's cutoff frequency, but simplifies the design equation for the outer loop.

In other words, the current controllers implemented in the following sections of this study are not only purposed with regulating the MMC arm current, but also contribute to shaping the loop gain of the power regulator. Since the primary loop gain is potentially dependent on the specific implementation of the current controller, the pole approximation will need to be independently verified for each case.

2.1.3 TIME-DELAY APPROXIMATION

It is important to consider that the implementation of this system will be in the discrete-time domain. The inclusion of a delay associated with the modulation and computational time due to the discrete nature of the system should be taken into account when determining the system's loop gains. Since the Laplace domain representation of a time delay is irrational, an approximation can be used to represent the delays in a ratio of polynomials form. Equation (16) demonstrates the first order Padé approximation of a time delay caused by a digital PWM implementation.

$$G_{PWM}(s) \approx e^{-s\frac{T_{samp}}{2}} \approx \frac{1 - s\frac{T_{samp}}{4}}{1 + s\frac{T_{samp}}{4}} \tag{16}$$

T_{samp} is the sampling period. The digital PWM delay, $G_{PWM}(s)$, is approximated by assuming there is an average delay of half the sample time because the carrier waveforms are triangular, so the modulator updates the output twice per sample period.

2.2 SYNCHRONOUS PI CONTROLLER

The first type of current controller implemented in this study is a proportional-integral (PI) controller in the *dq,* or synchronous, frame. The control diagram is shown in Figure 2.6.
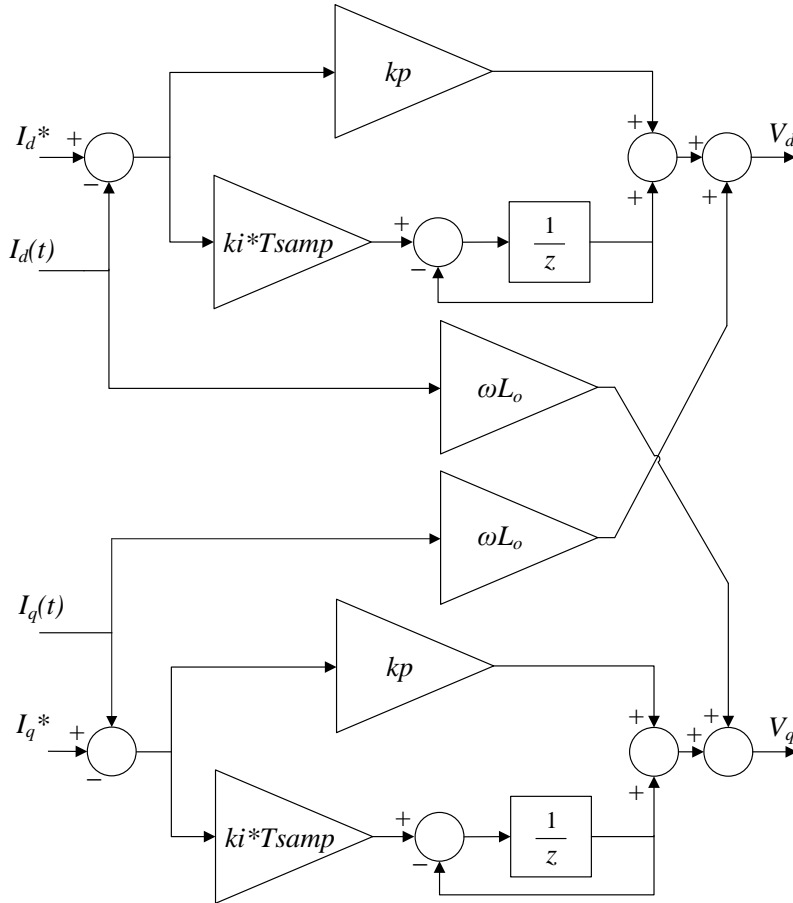

Figure 2.6 Decoupled *dq*-frame PI controller

An important characteristic of using a PI controller in the synchronous reference frame is that unlike the natural *abc* frame quantities of voltage and current, which are independent, the transformed quantities in the *dq* frame are dependent on each other. References [10] and [12] describe the dependencies between the two currents I_d and I_q. They two signals can be decoupled by feeding forward the common terms, as shown in the diagram.

The two reference voltages generated by the controller, V_d and V_q, are transformed back to the natural frame and sent to the modulator, where they are normalized according with the PSC-PWM method. The transfer function of the PI controller is given by (17). The open-loop transfer function of the inner current control loop is shown in (18).

$$G_{PI}(s) = \frac{V_d(s)}{e_{i,d}(s)} = \frac{sk_p + k_i}{s} \tag{17}$$

$$G_{O_1}(s) = G_{MMC}(s) * G_{PI}(s) = \frac{sk_p + k_i}{s^2 L_o + s R_o} \tag{18}$$

The transfer function $G_{MMC}(s)$ used in the control design was defined previously in (10).

It is possible to tune the PI controller coefficients by analyzing the closed-loop transfer function directly. Once put into the standard form of a second order system, the desired damping ratio can be chosen by selecting appropriate values for coefficients k_p and k_i. If each of the current control implementations can be tuned to obtain the so-called technical optimum damping coefficient of $\zeta = 1/\sqrt{2} \approx 0.707$, it will provide the means for a more comparable study. The closed-loop transfer function is shown in (19), the standard form of a second order system is shown in (20), and the modified closed-loop equation in (21).

$$G_{CL_1}(s) = \frac{G_{O_1}(s)}{1 + G_{O_1}(s)H(s)} = \frac{sk_p + k_i}{s^2 L_o + s(R_o + 2k_p) + k_i} \tag{19}$$

$$G(s) = \frac{K\omega_n^2}{s^2 + 2\zeta\omega_n s + \omega_n^2} \tag{20}$$

$$G_{CL_1}(s) = \frac{\dfrac{k_i}{L_o}}{s^2 + s\dfrac{(R + k_p)}{L_o} + \dfrac{k_i}{L_o}} + \frac{s\dfrac{k_p}{L_o}}{s^2 + s\dfrac{(R + k_p)}{L_o} + \dfrac{k_i}{L_o}} \tag{21}$$

The feedback loop is considered to have unity gain, so $H(s) = 1$; ζ and ω_n are the system's damping coefficient and natural frequency, respectively. Relating the coefficients in (20) and (21), the resulting equations for each of the control coefficients are shown in (22) and (23).

$$k_p = 2\zeta\omega_n L_o - R_o \tag{22}$$

$$k_i = L_o\omega_n^2 \tag{23}$$

Notice that the closed-loop equation in standard form has an overall DC gain of 2 and has two parts, one consisting of just the DC gain and the other a derivative term with an additional DC gain of $\frac{k_p}{k_i}$. The derivative term is parasitic, and can be prefiltered by adding a real pole to the system at $\omega = \frac{k_i}{k_p}$ to cancel its effects. A prefilter may not be required, depending on the values of the user defined coefficients, k_p and k_i, because the parasitic zero may be high enough as to not noticeably affect the closed-loop system in its operating frequency range.

The open-loop gain and phase margins of $G_{O_1}(s)$ are shown in Figure 2.7. The damping ratio and natural frequency are chosen as: $\zeta = \frac{\sqrt{2}}{2}$; $\omega_n = 2\pi 600$.
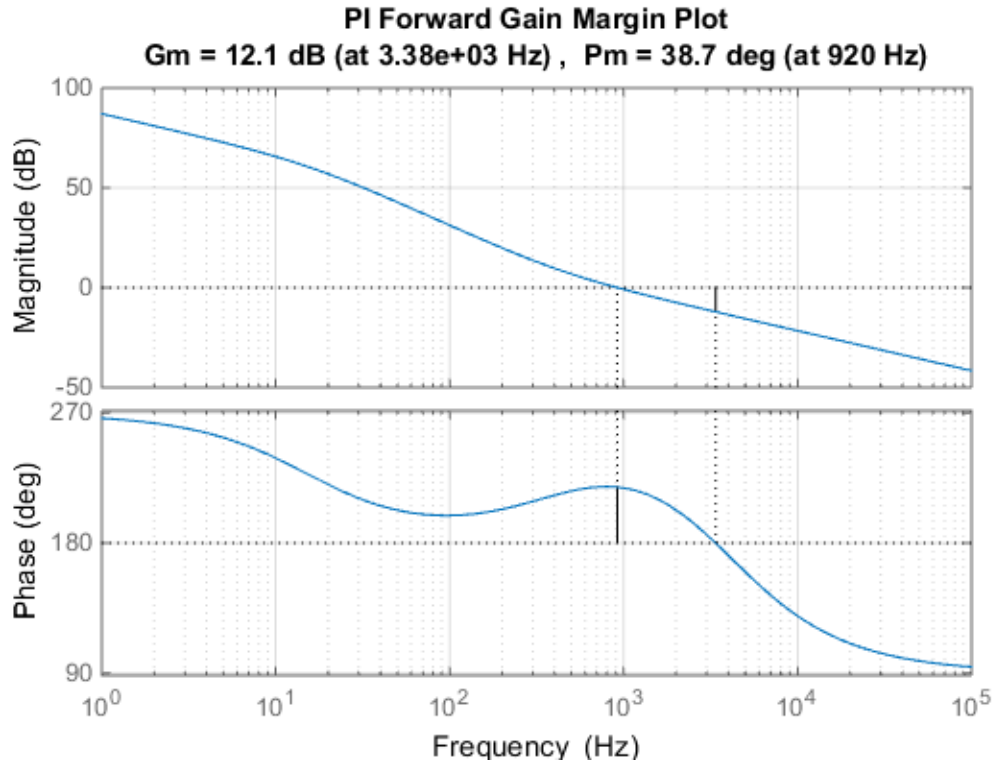
Figure 2.7 Technical optimum PI controller open-loop margin plot

The positive gain and phase margins indicate that the inner loop will be stable once the loop is closed. In the above plot, the digital PWM delay has been included in the closed loop transfer function. The additional term add phase lag at the sampling frequency and effectively just lowers the gain and phase margins. This yields more accurate results when comparing the simulation to the design, because the digital PWM delay will be present in the simulation.

The closed-loop frequency response is shown in Figure 2.8.
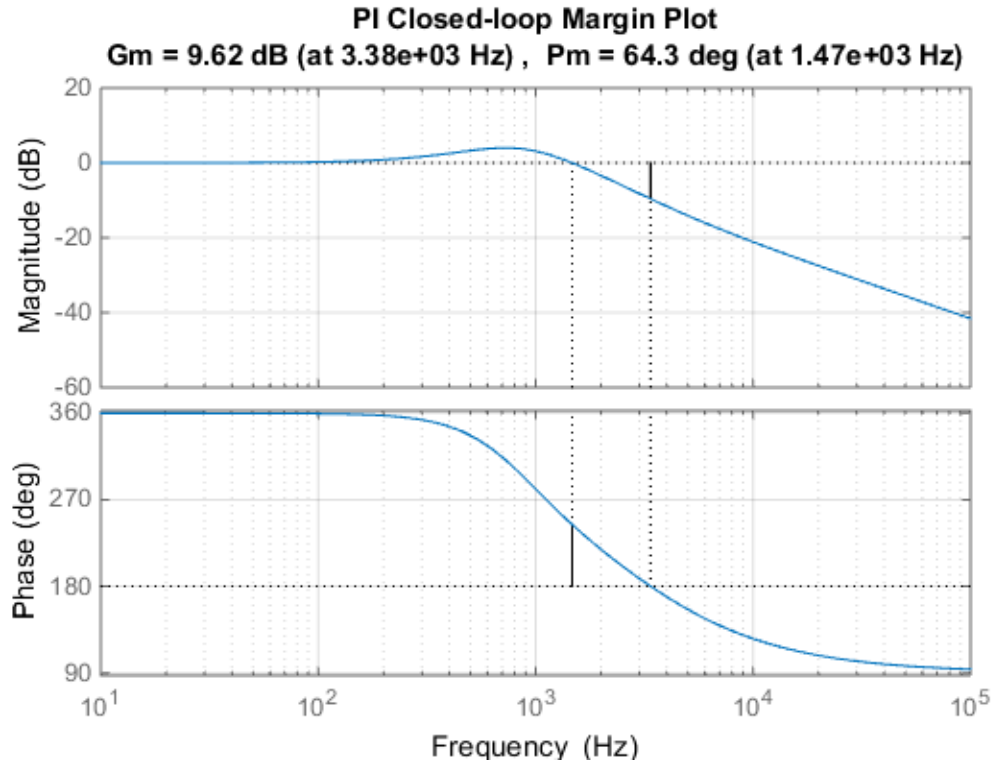
Figure 2.8 Technical optimum PI controller closed-loop Bode plot

The system's closed-loop crossover frequency is 1470 Hz, which exceeds the minimum bandwidth requirements of 600 Hz. There is, however, a quality factor (Q) greater than 1, which makes the approximation of representing the inner loop as a real pole in the primary loop inaccurate. A prefilter is added to negate the effects of the aforementioned parasitic derivative term, and the results are superimposed onto the original response in Figure 2.9.
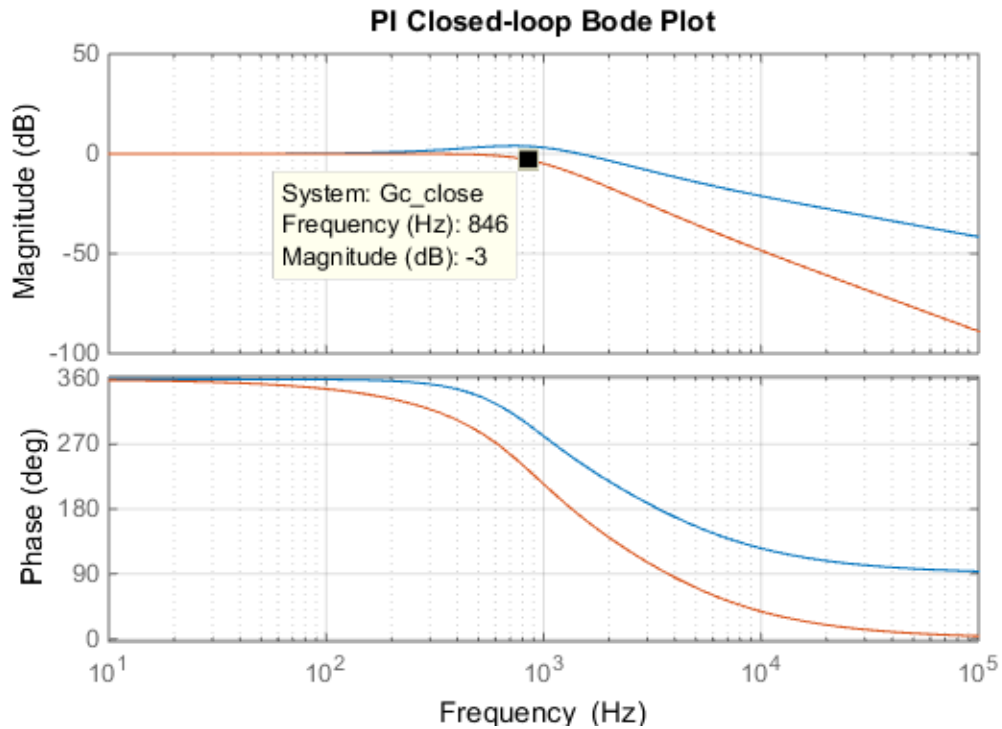
Figure 2.9 PI closed-loop response comparison
(Blue – no prefilter, Red – prefilter)

The frequency response clearly shows an improved Q and a bandwidth of 846 degrees, which meets the minimum bandwidth requirements. This system can now accurately be approximated by a single real pole at 846 Hz. The phase shift at the outer loop's crossover frequency is 8 degrees, which is fairly small and can be considered negligible.

Finally, the step responses of the system with and without the prefilter are shown in Figure 2.10.

Figure 2.10 Technical optimum PI control step response
(Blue – no prefilter, Red – prefilter)

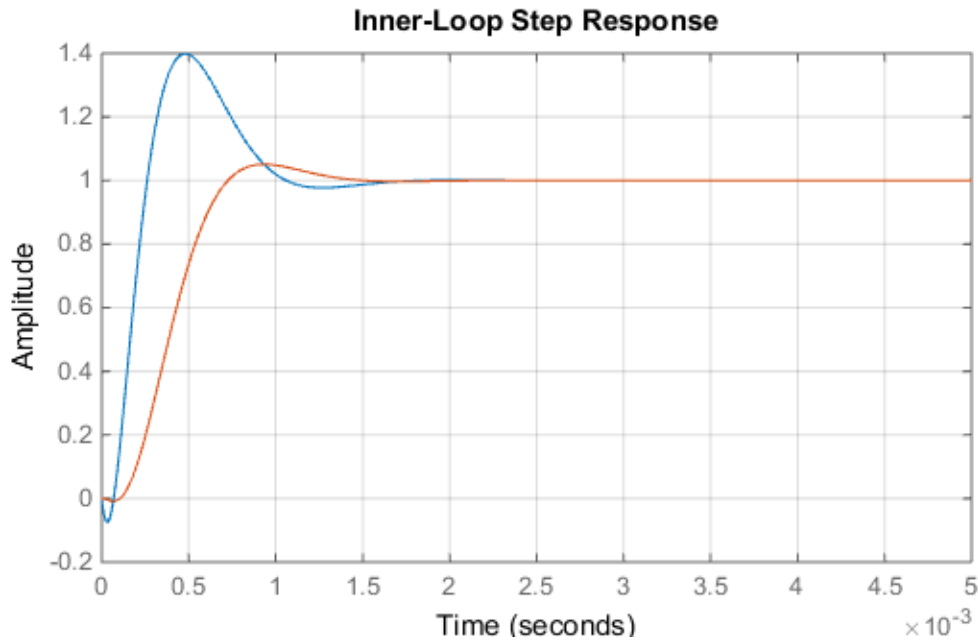The system without the prefilter is shown in blue and the response after the prefilter is added is shown in red. The settling time for both is nearly identical, but the prefilter lowers the overshoot by about 35% from 40% to about 5%. This overshoot more appropriately represents the desired damping ratio of 0.707.

2.2.1 ALTERNATIVE TUNING METHOD (PI)

It is also possible to design the PI controller coefficients based on a desired crossover frequency and phase margin. This is done by analyzing the open-loop transfer function shown previously in (18). From the open-loop frequency response characteristics, the proportional (k_p) and integral (k_i) coefficients can be calculated as shown in (24) and (25),

$$k_p = \frac{1}{|G_{O_1}(j\omega_c)|} \cos(\pi + \phi_m - \phi_c) \tag{24}$$

$$k_i = -\frac{j^2\omega_c}{|G_{O_1}(j\omega_c)|}\sin(\pi + \phi_m - \phi_c) \qquad (25)$$

where ω_c is the desired closed-loop crossover frequency, ϕ_m is the desired phase margin of the closed-loop system, and ϕ_c is the phase quantity of $G_{O_1}(s)$ at the desired crossover frequency. As a general rule, a phase margin of 60 degrees allows for a desirable system response. This usually gives a fast settling time with minimal ringing. Since the crossover frequency for the inner current loop in this application should be at least ten times higher than outer voltage loop, a crossover frequency of 600 Hz is used.

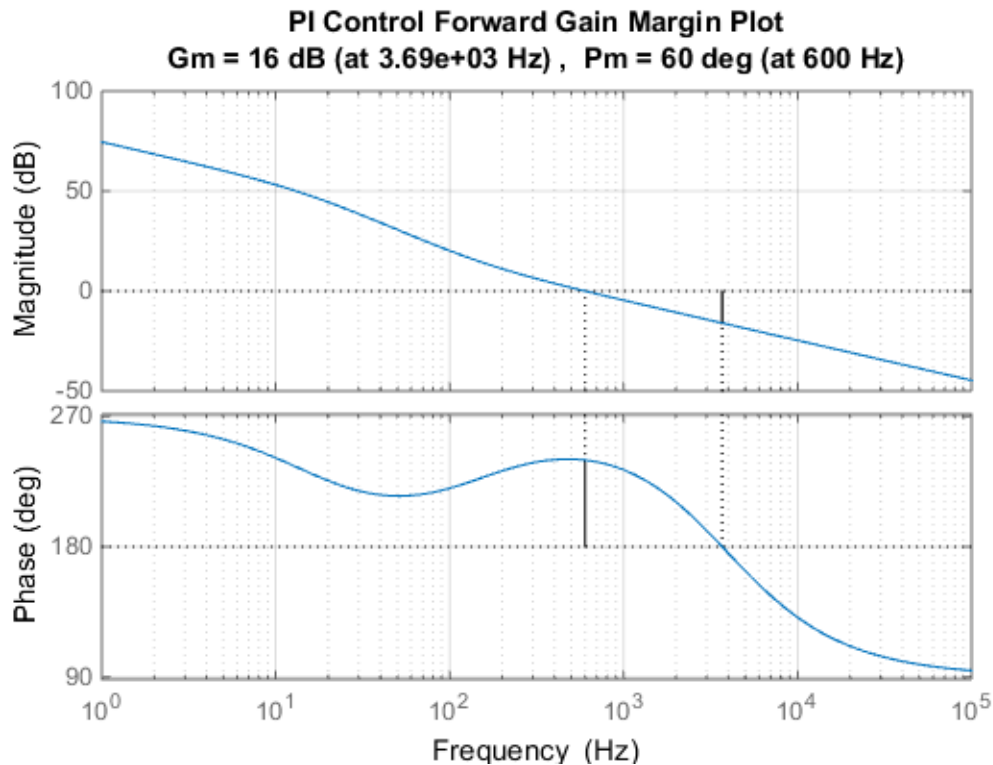The forward loop phase and gain margins are shown in Figure 2.11.

Figure 2.11 Alternative PI controller open-loop margin plot

The positive gain and phase margins indicate stability when the loop is closed, and the 60 degree phase margin should ensure a desirable step response. The crossover frequency is exactly 600 Hz.

The closed-loop transfer function is shown in (26), and the frequency response is shown in Figure 2.12.

$$G_{cl}(s) = \frac{I_d(s)}{I_d^*(s)} = \frac{sk_p + k_i}{s^2 L_o + s(R + 2k_p) + k_i} \tag{26}$$
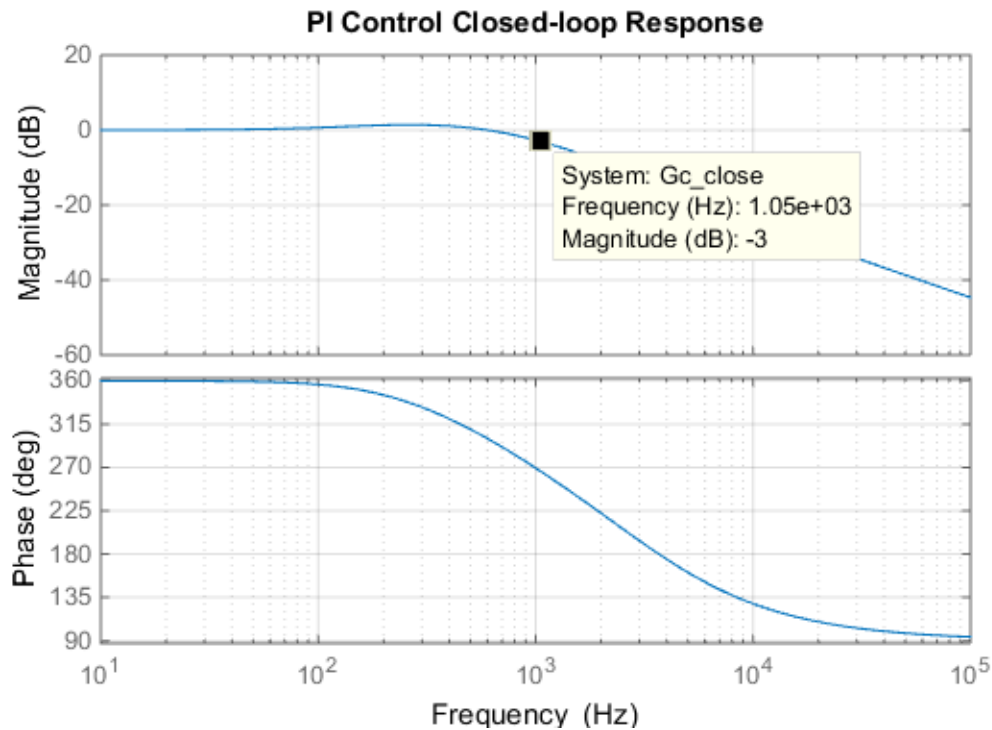

Figure 2.12 PI controller closed-loop Bode plot

Finally, the step response of the controller is shown in Figure 2.13. The response from the technical optimum tuning method is superimposed on the plot to show a comparison, where the technical optimum method is shown in red and the alternative tuning method is shown in blue. The alternative method plot shows a slightly slower rise

time and longer settling time, but reduces the overshoot to about 18%. Of course, the chosen crossover frequency and phase margin may be tuned to provide a more desirable response. The prefilter is not included for this comparison.
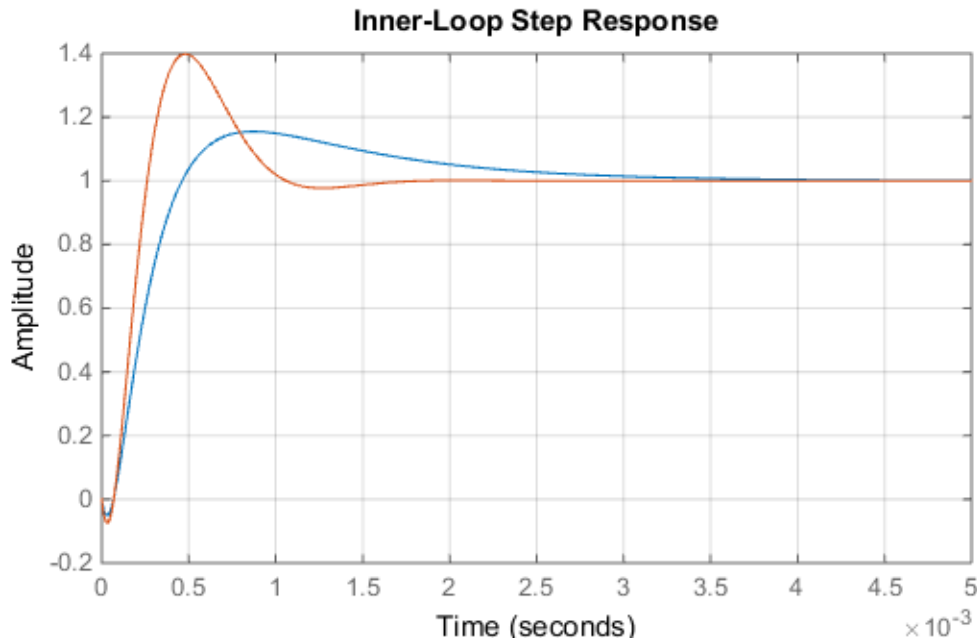
Figure 2.13 PI controller closed-loop step response
(Red – Technical optimum, Blue – Alternative)

2.3 PROPORTIONAL RESONANT CONTROLLER

The second current controller to be implemented is a proportional resonant (PR) controller in the natural (abc) frame. The major disadvantage of the synchronous PI control is the necessity of a dq transformation to achieve zero steady-state error for an oscillatory reference. With PR control, there is a resonant term that provides a high gain at a specified resonant frequency band. It is operationally similar to the PI, but does not need the complex coordinate transformation to track a sinusoidal reference. The PR control scheme is shown in Figures 2.14 (a) and (b), as described in [14].

31
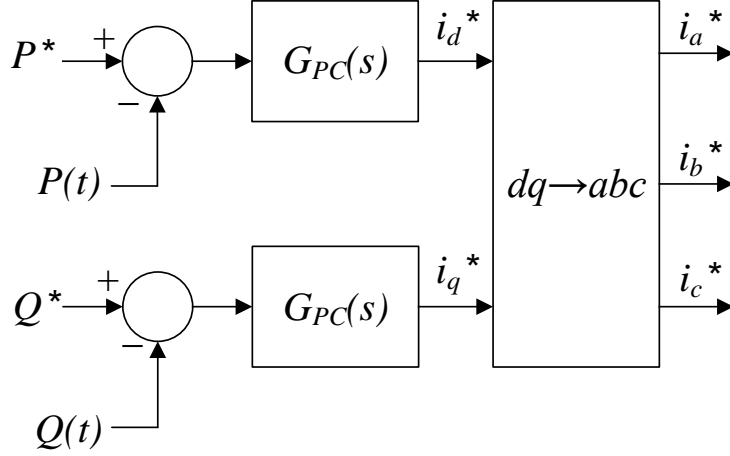
(a)
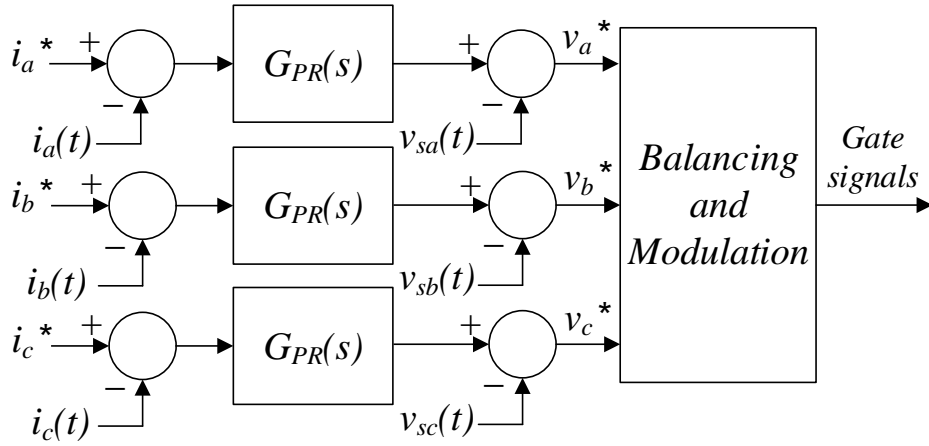
(b)

Figure 2.14 PR outer power (a) and inner current (b) control diagrams

The reference voltages generated v_a^*, v_b^*, and v_c^* are shifted and normalized as according

to the PSC-PWM method. The general form of an ideal PR controller is shown in (27),

$$G_{PR}(s) = \left(k_p + \frac{s k_r}{s^2 + \omega_o^2}\right) \tag{27}$$

where k_p is the proportional gain and k_r and ω_o are the resonant gain and frequency,

respectively. In general, k_p determines the controller dynamics, while k_r determines the

system's amplitude gain at the resonant frequency and controls the width of the

frequency band [15]. Figures 2.15 (a) and (b) show the effects of altering one coefficient while holding the other constant.
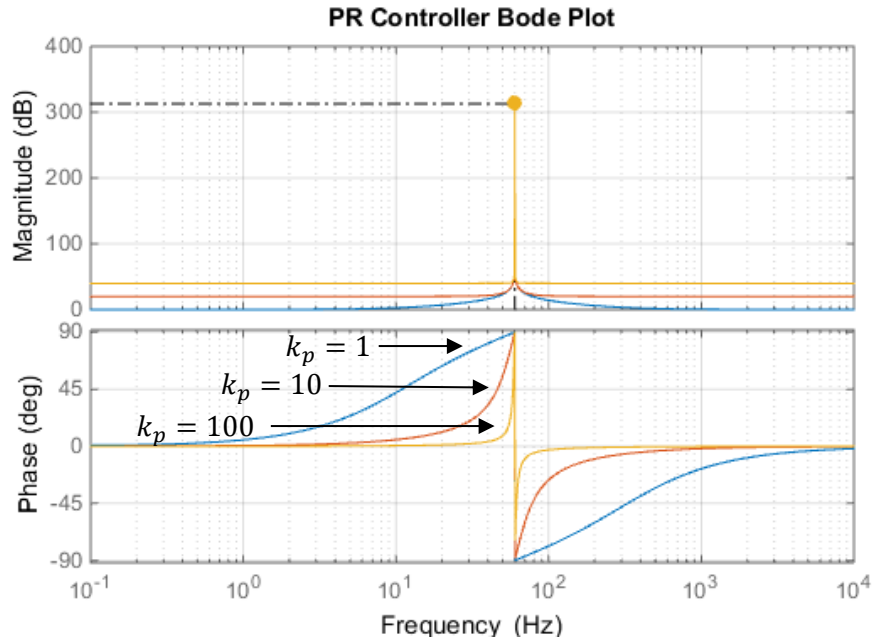
(a) $k_r = 1000$, varying k_p
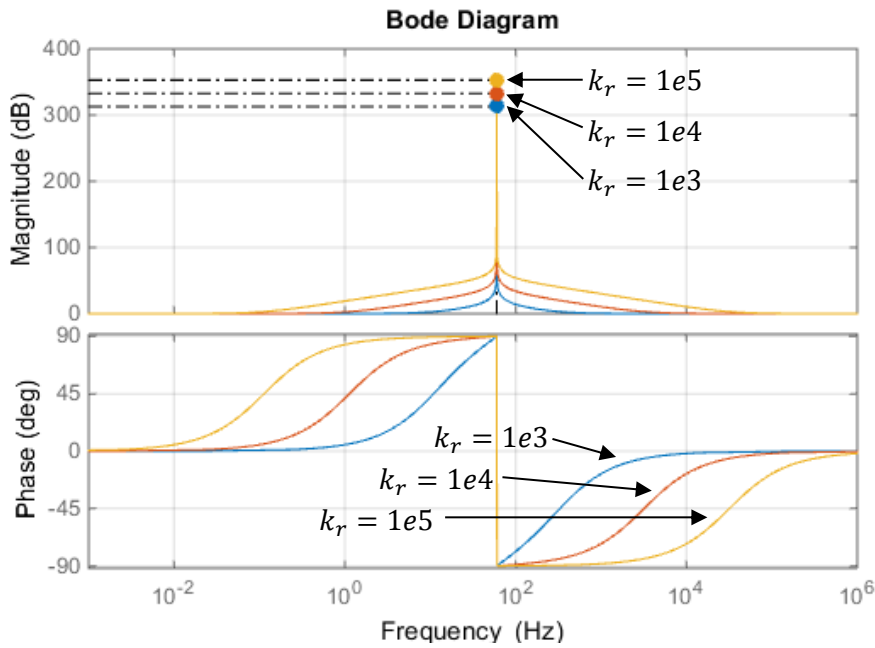
(b) $k_p = 1$, varying k_r

Figure 2.15 (a) and (b) PR coefficients comparison

Equations (10) and (27) make up the open-loop transfer function of the inner loop in (28).

$$G_{O_2}(s) = G_{MMC}(s) * G_{PR}(s) = \left(\frac{1}{R_o + sL_o}\right)\left(k_p + \frac{sk_r}{s^2 + \omega_o^2}\right) \tag{28}$$

2.3.1 NASLIN POLYNOMIAL CONTROLLER DESIGN

The design method for tuning the PR controller coefficients is not as straight forward as a PI controller, since the addition of the resonant term results in a third order open-loop system transfer function. The difficulty here lies in extracting a description of the damping coefficient, which is necessary for this analysis. Many different design methods have been proposed, like the ones in [14] and [15]. One method for this design procedure is based on the usage of Naslin polynomials, the method of which is described in more detail in [16]. From the open-loop transfer function, the canonical form of the characteristic equation will be: $P(s) = a_n s^n + a_{n-1} s^{n-1} + \cdots + a_1 s + a_0$. Each of the coefficients of the polynomial are essentially used to set the time constant (τ) and characteristic ratio (α). The formulas for the time constant and characteristic ratio of a second order characteristic polynomial are shown in (29) and (30) [16].

$$\tau = \frac{a_1}{a_0} \tag{29}$$

$$\alpha = 4\zeta^2 \tag{30}$$

It is now possible to design the coefficients to yield the technical optimum damping coefficient of $\zeta = \frac{1}{\sqrt{2}}$, by choosing a characteristic ration of $\alpha = 2$ [18]. The closed-loop transfer function of the system is shown in (31).

$$G_{O2}(s) = \left[\frac{s^2 k_p + sk_r + k_p\omega_o^2}{s^3 L_o + s^2(R_o + k_p) + s(L_o\omega_o^2 + k_r) + (R_o\omega_o^2 + k_p\omega_o^2)}\right] \tag{31}$$

34

The third order characteristic polynomial in canonical Naslin form is shown in (32).

$$N(s) = a_0 \left(1 + s\tau + s^2 \left(\frac{\tau^2}{\alpha} \right) + s^3 \left(\frac{\tau^3}{\alpha^3} \right) \right) \tag{32}$$

Comparing (31) and (32), the coefficients can be compared to achieve (33) [16].

$$\tau = \frac{\sqrt{\alpha}}{\omega_o} \qquad k_p = \left(L_o \left(\frac{\alpha^2}{\tau} \right) - R_o \right) \qquad k_r = L_o \left(\frac{\alpha^3}{\tau^2} - \omega_o^2 \right) \tag{33}$$

The Bode plot of the open-loop system is shown below in Figure 2.16.
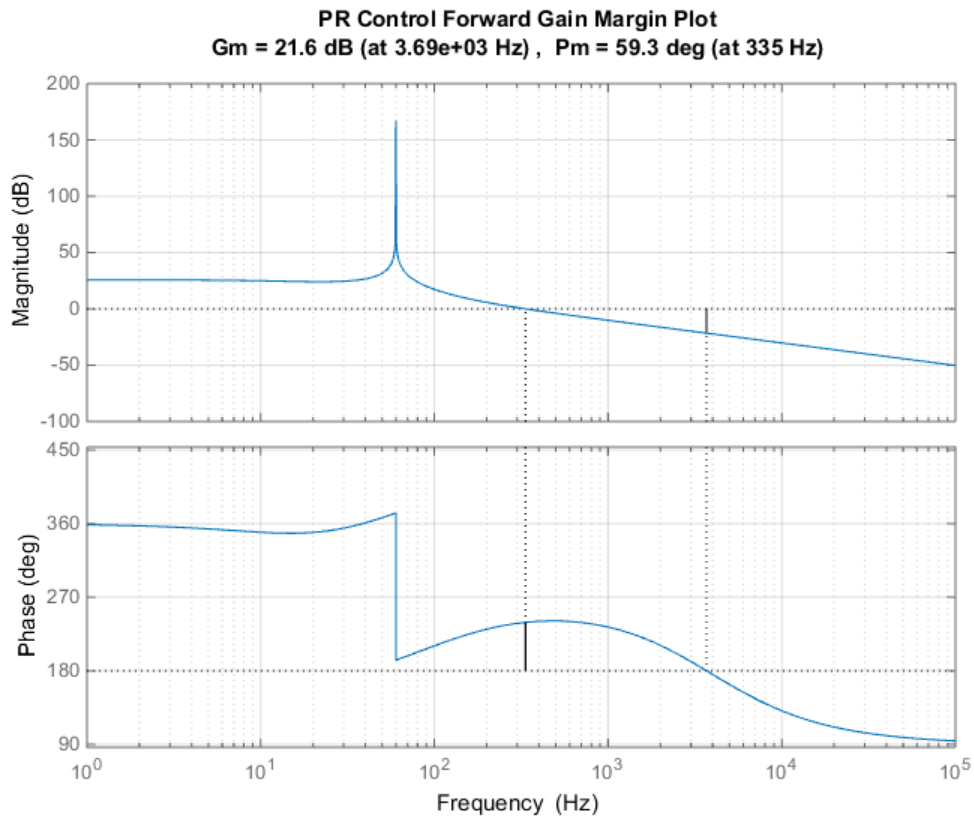

Figure 2.16 Technical optimum PR controller open-loop margin plot

The crossover frequency of the PR controller is a good bit lower than the technical optimum PI controller design, but in order to adhere to the guidelines of this comparison,

the damping coefficients must be equivalent. The controller coefficients may be tuned to improve the dynamic response if necessary.

The closed-loop response is shown in Figure 2.17.
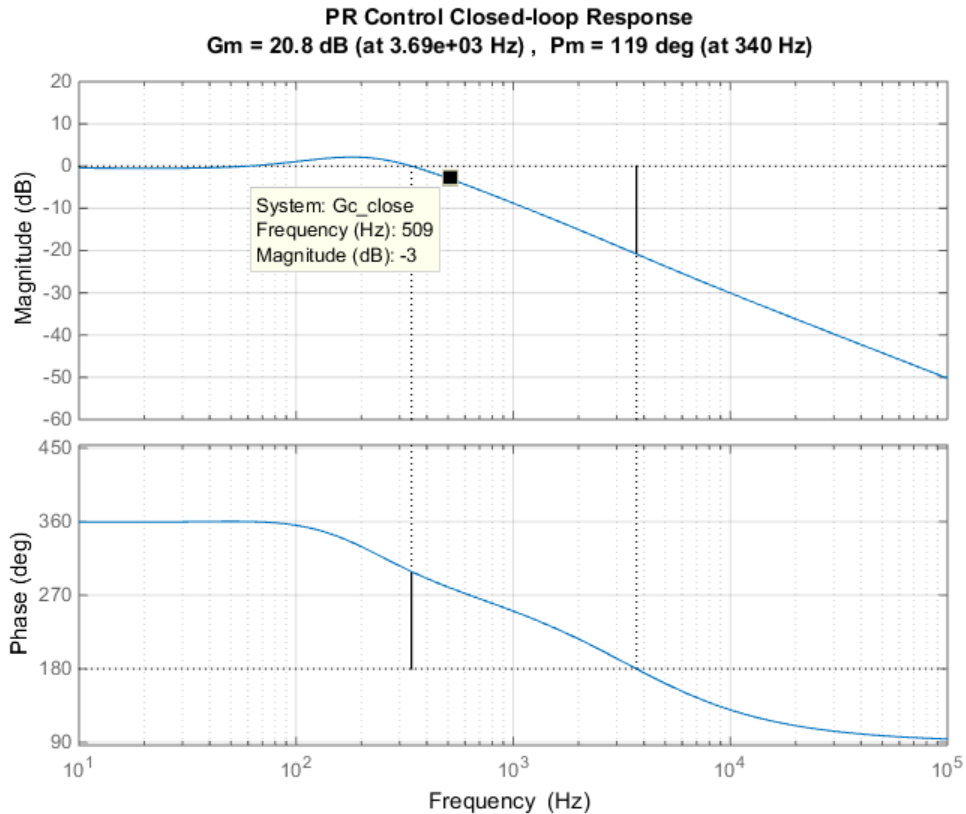
Figure 2.17 Technical optimum PR closed-loop bode plot

2.3.2 ALTERNATIVE TUNING METHOD (PR)

Because the PI and PR controllers are operationally identical and related via Park's transformation, the control coefficients for each transfer function are also related. As described in [7], the proportional coefficient k_p for the PR controller implementation is chosen based on the desired crossover frequency, which is exactly the same for the conventional PI control. The resonant coefficient can be determined by taking the

Laplace transform of the rotating reference PI controller, considering both the direct and reverse sequence transformations. The result is shown in (34).

$$F_o(s) = \frac{k_i}{s + j\omega_o} + \frac{k_i}{s - j\omega_o} = \frac{2k_i s}{s^2 + \omega_o^2} \tag{34}$$

Since the controller's closed-loop crossover frequency is much higher than ω_o, $F_o \approx \frac{2k_i}{s}$, which can now be compared to the conventional PI controller's integral term. Relating (34) to (27), the resonant coefficient can be determined to be $k_r = 2k_i$. The Naslin polynomial method is used in this thesis because it yields better operational results in simulation than the alternative method.

2.4 PREDICTIVE CONTROLLER

The third current control method implemented in this study is called digital deadbeat, or predictive control. Unlike the PI and PR controllers that accumulate integral error, deadbeat control is a method that attempts to predict the control action needed during each sample interval through calculations based on both the circuit model of the system being controlled and that system's feedback signal(s). The ability to bring the system output to the reference value is dependent entirely on the accuracy of the circuit model. Just like the other digital approaches, the time required to calculate the controller's output for the next time step is a delay of one sample interval, T_{samp}. In addition to a calculation delay, there is also a delay caused by the modulation. Since the system output cannot reach the commanded value until the modulator reacts to the reference signal change, the controller needs to calculate the predicted control action needed two time steps in advance [7].

Each of the six arm currents are the controlled quantities in this method. The equations for the total current flowing through each of the positive-side and negative-side arm inductors are rewritten in (35) and (36).

$$I_{pj} = \frac{i_j}{2} + \frac{I_{dc}}{3} + i_{zj} \tag{35}$$

$$I_{nj} = -\frac{i_j}{2} + \frac{I_{dc}}{3} + i_{zj} \tag{36}$$

The term i_j is the AC-side current being supplied by the grid, I_{dc} is the DC-side current flowing through all arms of the converter, and i_{zj} is the unwanted circulating current flowing in phase unit j [17]. Since there are two arms per phase, each one will have half of the total phase current i_j; because there are three phases sharing the total DC current, there is one third of I_{dc} in each arm. By determining an appropriate arm current reference for all six of the arm inductors and utilizing an accurate deadbeat control algorithm, the unwanted circulating current i_{zj} can be effectively reduced. Because of the complexity of the converter, some approximations are made that produce some error in the deadbeat controller's tracking, however the unwanted circulating current will be significantly reduced. This is the main advantage of this control approach.

The control design approach is relatively straight forward. At any control iteration, or at every sample instant, the average output voltage should be determined that causes the average inductor current to reach its reference by the end of the modulation period. The equivalent circuits of the phase j upper and lower arms are shown in Figure 2.18 (a) and (b).

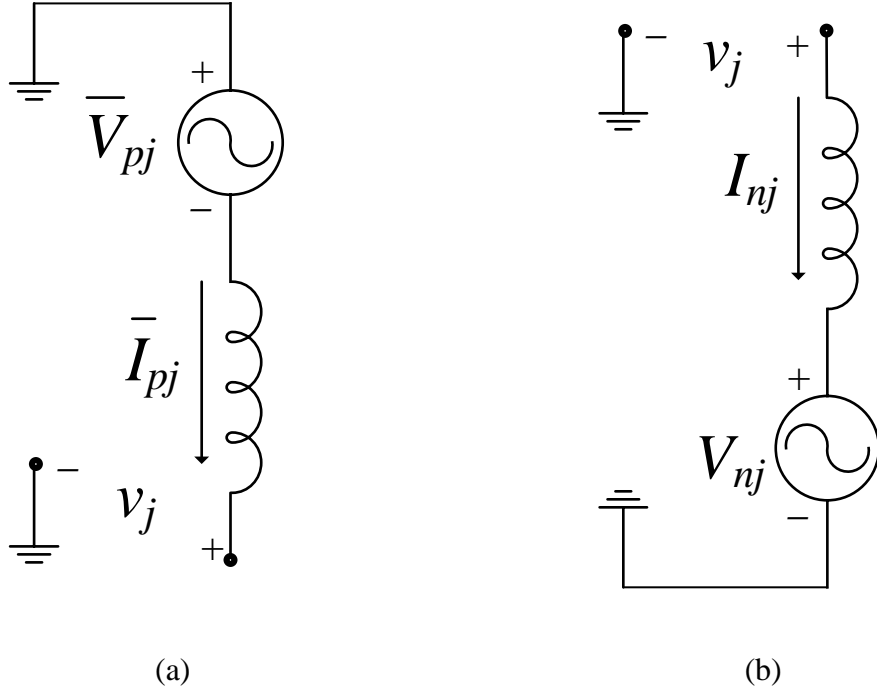<center>(a)   (b)</center>

<center>Figure 2.18 Upper (a) and lower (b) arm deadbeat control equivalent circuit</center>

From this approach, the control equation for the upper and lower arms can be derived using the equivalent circuit and the average values of V_{pj}, V_{nj}, I_{pj}, and I_{nj} as shown in (37) and (38) [7].

$$\overline{I_{pj}}(k+1) = \overline{I_{pj}}(k) + \frac{T_{samp}}{L}\left[\overline{V_{pj}}(k) - v_j(k)\right] \tag{37}$$

$$\overline{I_{nj}}(k+1) = \overline{I_{nj}}(k) + \frac{T_{samp}}{L}\left[v_j(k) - \overline{V_{nj}}(k)\right] \tag{38}$$

Sample 'k' denotes the value at the present sample interval, while the next sample interval is denoted 'k+1'. As previously described, the target inductor current will need to be calculated two time steps in advance, so the equation for the positive arm can be rewritten one step forward in (39).

$$\overline{I_{pj}}(k+2) = \overline{I_{pj}}(k) + \frac{T_{samp}}{L}\left[\overline{V_{pj}}(k+1) + \overline{V_{pj}}(k) - v_j(k+1) - v_j(k)\right] \tag{39}$$

<center>39</center>

The equation can be simplified further by assuming that the phase voltage v_j is a slowly varying quantity in comparison to the sampling frequency and modulation period. Equation (39) can be rewritten considering $v_j(k + 1) \approx v_j(k)$ [7]. The same steps are taken for the negative arm, and equations for the control variables V_{pj} and V_{nj} can be determined in (40) and (41).

$$\overline{V_{pj}}(k + 1) = \frac{L}{T_{samp}}\left[\overline{I_{pj}}(k + 2) - \overline{I_{pj}}(k)\right] - \overline{V_{pj}}(k) + 2v_j(k) \tag{40}$$

$$\overline{V_{nj}}(k + 1) = -\frac{L}{T_{samp}}\left[\overline{I_{nj}}(k + 2) - \overline{I_{nj}}(k)\right] - \overline{V_{nj}}(k) + 2v_j(k) \tag{41}$$

This control equation can be inserted directly into the control model, where the measured quantities are the phase voltage v_j and the arm current I_p. $I_{pj}(k + 2)$ is the desired arm current at sample time (k+2), which can be replaced by $I_{refj}(k)$ and $V_{pj}(k)$ is the control output voltage calculated during the previous iteration. The reference voltages V_{pj} will be shifted and normalized according to the PSC-PWM method. This normalization makes an assumption that the DC-bus voltage is known and constant, which may not be the case; this will be discussed in more detail later in this study.

The only tunable parameters of the controller are the selections of the assumed arm inductance L and the sample time T_{samp}. It is clear that the optimal tuning for the controller would be a value of L that is exactly matched to the actual arm inductance L_o, and a value of T_{samp} that exactly matches the modulation period.

CHAPTER 3

SIMULATION RESULTS AND COMPARISON

Each of the three current controllers are designed as described in Chapter 2 using

MATLAB and then inserted into a Simulink model of a MMC. Unless otherwise stated,

the MMC model is designed with the following parameters listed in Table 3.1.

Table 3.1 MMC System Parameters

Quantity	Value
Submodules per arm N	6
Carrier frequency f_c	500 Hz
Nominal Active Power P^*	60 kW
Nominal Reactive Power Q^*	0 Var
AC system nominal voltage v_{sj}	208 V$_{rms}$ (ph-ph)
AC system inductance L	0.1 mH
AC system resistance R	10 mΩ
AC system fundamental frequency f_o	60 Hz
Sample time T_{samp}	1.67e-4 s (6000 Hz)
DC system voltage V_{dc}	800 V
Submodule capacitance C_o	15 mF
Arm inductance L_o	0.7 mH
Arm resistance R_o	70 mH

All controller simulations will be evaluated using the same two test cases. First, in

order to validate the design process for each, the dynamics of the current controllers will

be tested independently. This is possible by breaking the outer loop, such that the power

regulator's output does not control the current controller's input. Instead, a current

reference is manually generated and a step change is applied to it. The initial and final

values of the current set point will be calculated based on an active power of 40 kW and 60 kW. Since the power regulator normally calculates the current reference in the dq frame, the manually generated reference can be easily applied if it is composed of dq quantities. Assuming a balanced system, the calculations for the two current references are shown in (42) and (43) using the Park transformation. Quantity I_q^* is 0A for all cases.

$$I_{d1}^* = \frac{2}{3}\left(\frac{40\ kW}{120\sqrt{2}}\right) = 157.1\ A \tag{42}$$

$$I_{d2}^* = \frac{2}{3}\left(\frac{60\ kW}{120\sqrt{2}}\right) = 235.5\ A \tag{43}$$

For the second test case, both loops will be included in the simulation so the entire system's performance can be observed. The system will be brought to steady-state operation with an active power set point of 40 kW, and then the set point will be increased to 60 kW. The reactive power set point will be 0 Var for all simulations. The transient response of the AC-side and DC-side power measurements will be shown so that the dynamic performance and converter efficiency can be quantified. The transient response of the phase currents will also be observed, and the performance difference between the three current controllers will be shown with plots of the phase current error $e_{ij}(t)$. Then, the three-phase circulating currents for each controller implementation will be measured and compared, such that the benefit of using the presented novel approach to predictive control is shown.

Lastly, the converter's AC-side output voltage is plotted to show synchronicity with the grid and the total harmonic distortion (THD) is measured and compared for each of the three controllers.

3.1 PI CONTROL SIMULATION

The control scheme for the synchronous PI controller is shown in Figure 3.1.
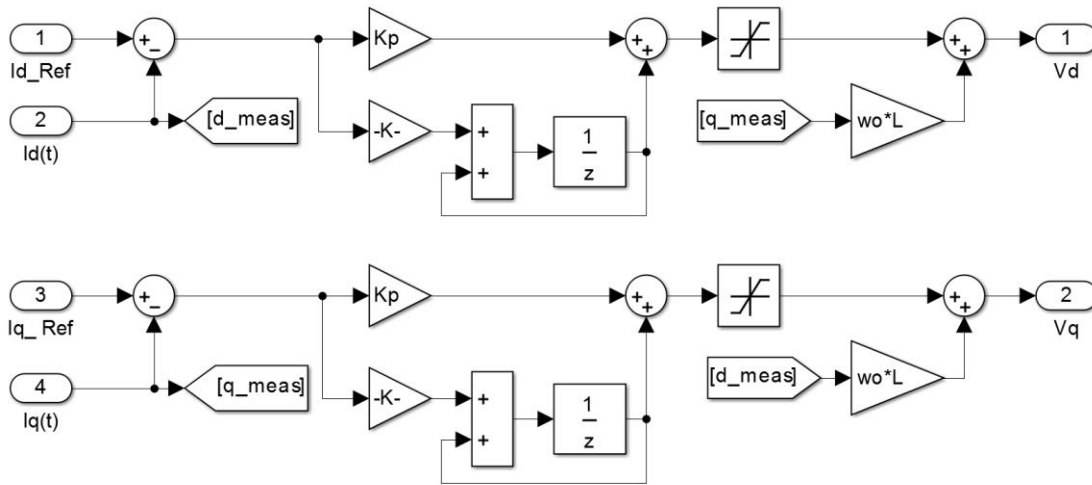

Figure 3.1 PI controller Simulink model (-K- = $Ki * T_{samp}$)

The controller parameters are calculated using the technical optimum method described

in section 2.2, with a k_p of 3.662 and a k_i of 9948.6. The PI current controller dynamics
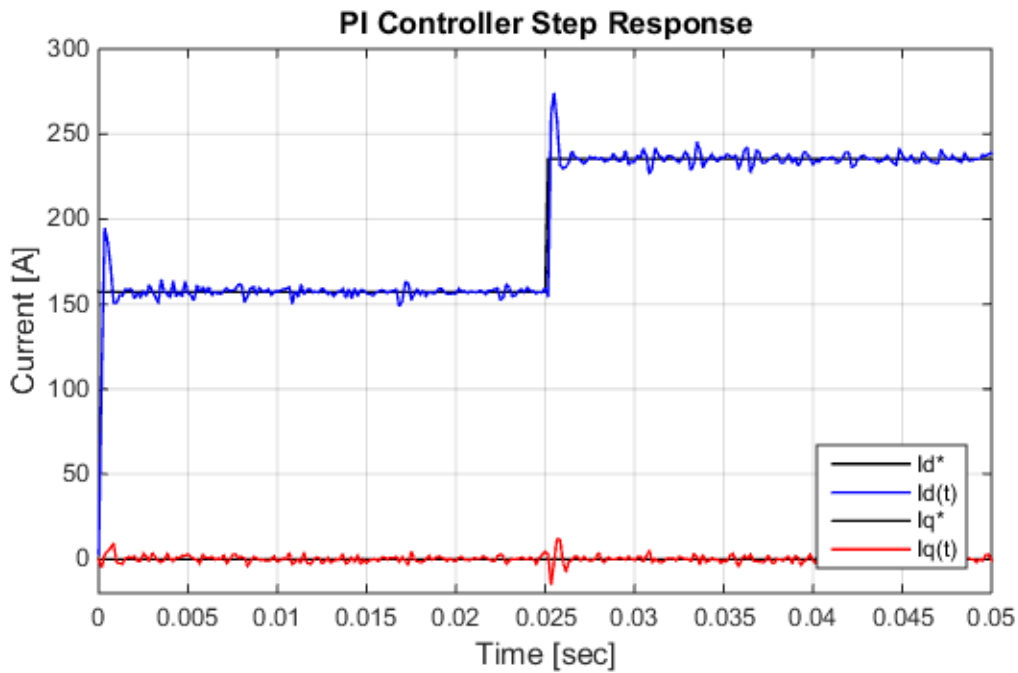
are shown in Figure 3.2.

Figure 3.2 PI controller simulation step response

The simulated controller dynamics are very close to the dynamics of the continuous-time design previously discussed, with a settling time of approximately 3 ms and an overshoot of around 20%. This confirms both the assumption that the sample time is small enough and validates the equivalent circuit model used in the design. These results also confirm that the PI control design for the inner loop is stable and fast enough for this system.

A prefilter can also be added to eliminate the overshoot caused by the parasitic derivative term previously discussed. The result after the prefilter is added is shown in Figure 3.3.
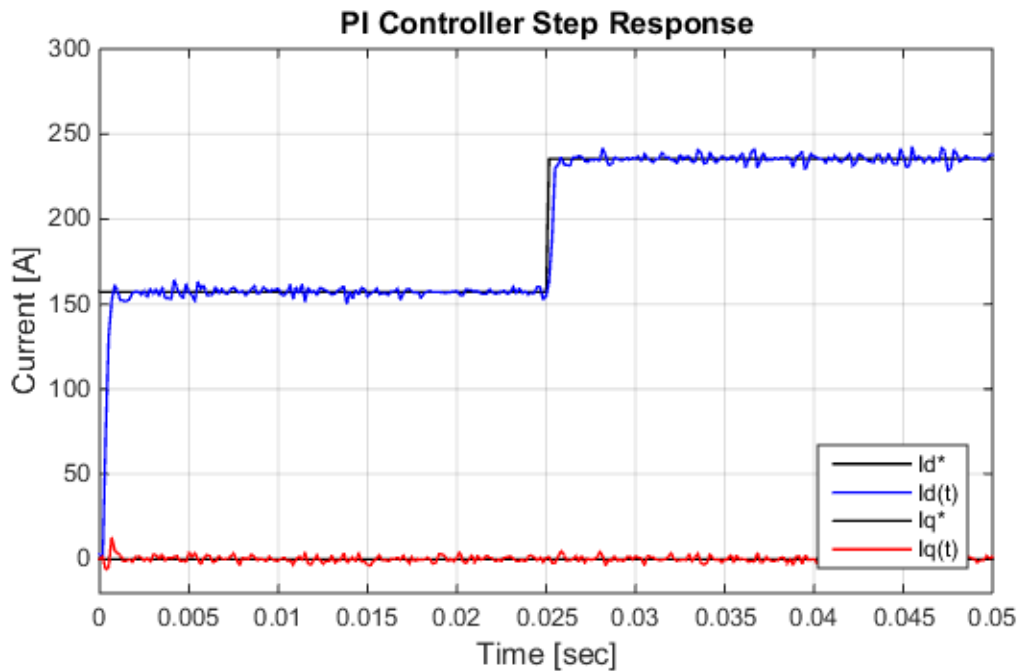

Figure 3.3 PI controller simulation step response (prefiltered)

The prefilter essentially removes some of the high frequency content present in the reference signal, effectively eliminating the system's overshoot. For this application, the current reference generated by the outer power loop will vary at a much slower rate, so the bandwidth of the inner loop is clearly sufficient and the prefilter is not required.

Now, the outer power regulation control is included in the loop and the entire system's operation can be analyzed. The dynamic response of the active power in each side of the converter is shown in Figure 3.4 below. The power set point is changed from 40 kW to 60 kW at 0.2 seconds.
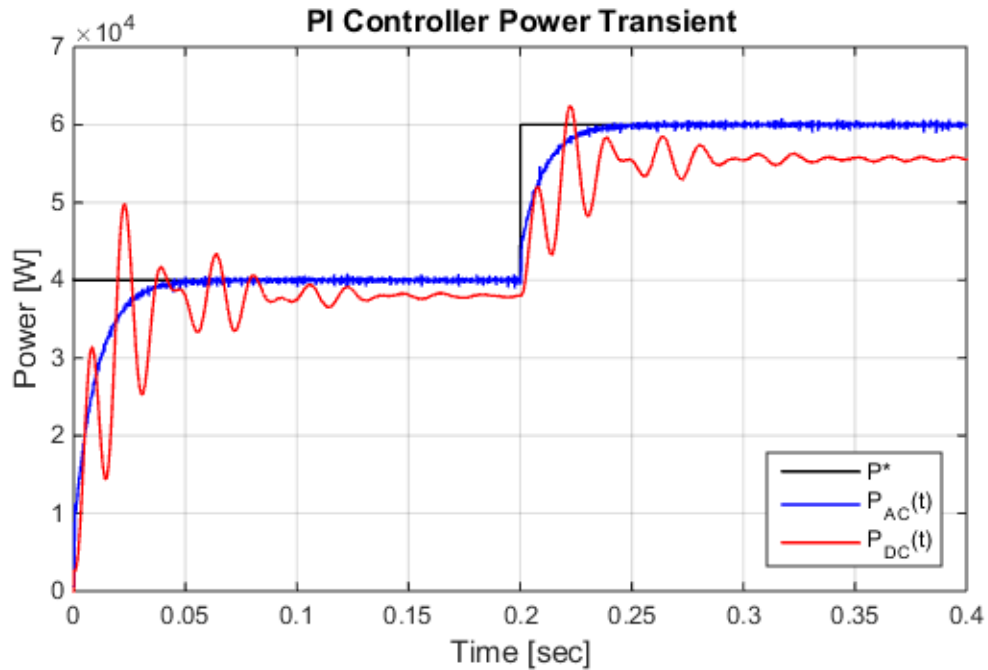

Figure 3.4 PI Controller AC and DC Power Transient

The converter's power losses are clearly visible, as the efficiency ranges from approximately 95-92.5% at the two set points. The settling time of the DC power for this implementation is about 75 ms.

The phase current i_a is shown in Figure 3.5 with the same power set point change being applied. For clarity, the plot is zoomed in around the step change. The ability of the PI controller to track the current reference is very good, and there is little to no deviance from the reference transient behavior during the step change due to the inner loop's bandwidth being sufficiently high.
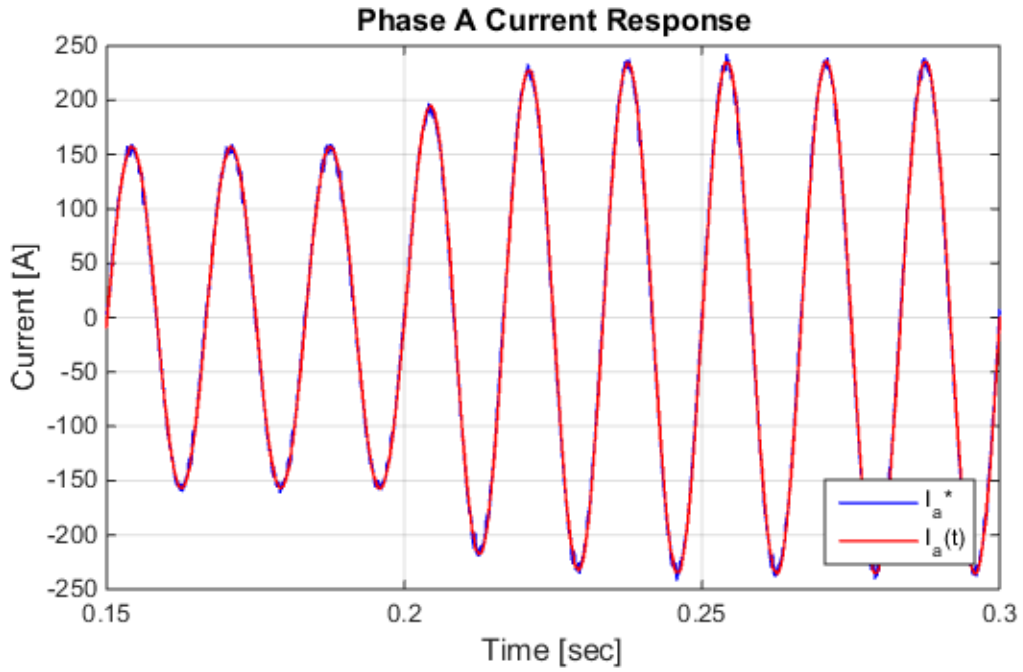
Figure 3.5 Phase a current tracking under PI control

The error between the reference and the measured current is shown in Figure 3.6.
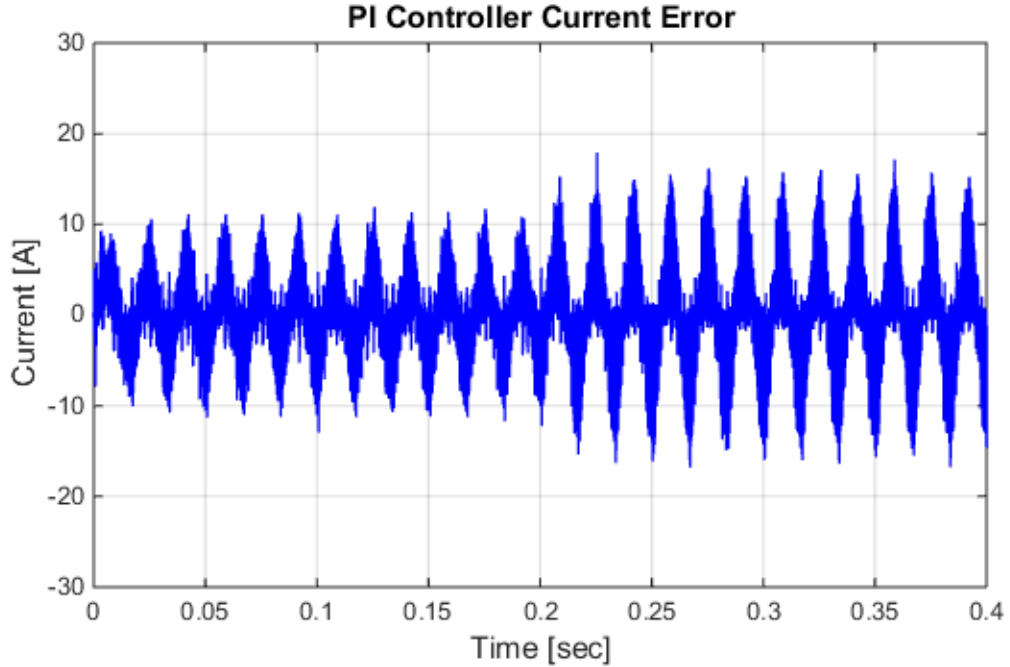

Figure 3.6 PI controller per-phase current error

The error has an approximate peak-to-peak amplitude of 19 A at 40 kW and 28 A at 60 kW. The error has a range of approximately 5.5-6% of the total phase current.

The circulating currents in all three phases of the converter are shown in Figure 3.7. The measurement is taking according to (8).
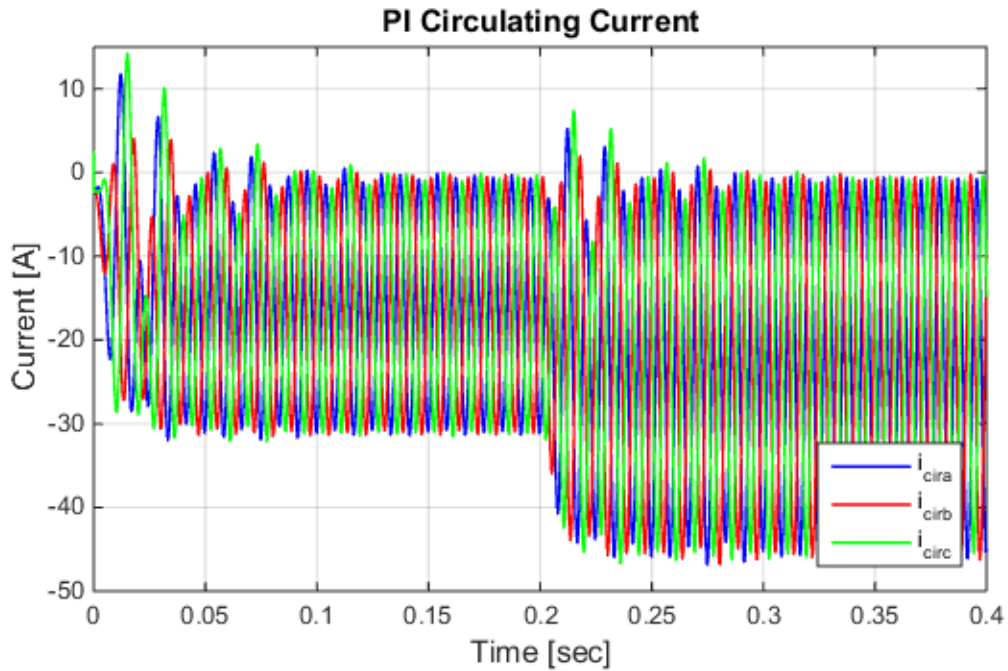

Figure 3.7 PI control circulating currents

The peak-to-peak magnitude of the circulating current's AC component for the two power references is approximately 30 A and 45 A, which are about 9.5% of the total phase current. The circulating currents' DC components are also clearly visible. Figure 3.8 shows four periods of the circulating current in steady state. The currents are double fundamental frequency and are sinusoidal, with the addition of very little high frequency content at the maximums.
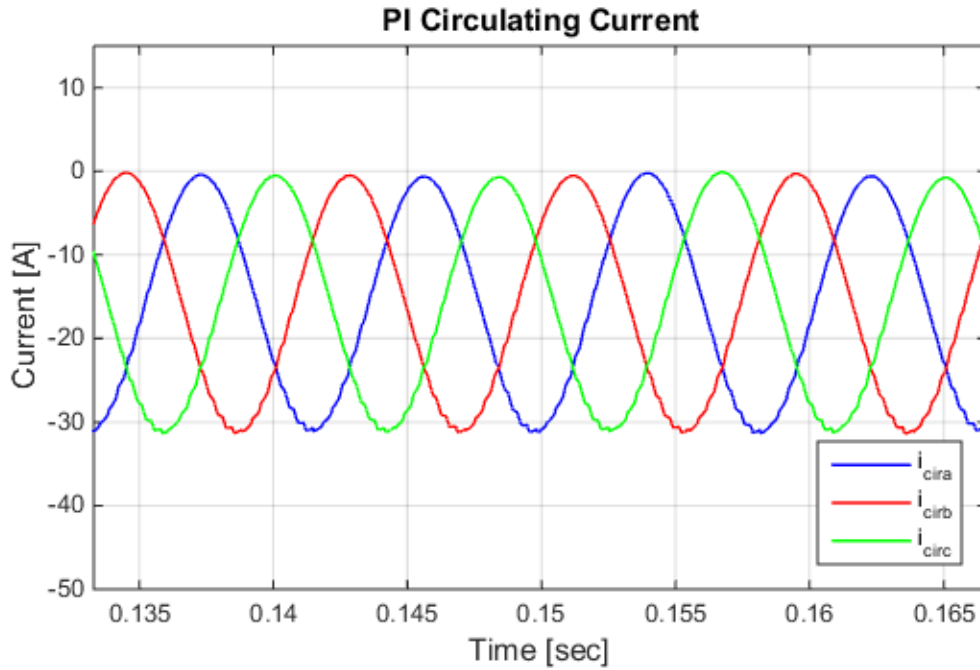
Figure 3.8 PI control circulating currents (zoomed)

Lastly, the converter's output voltage on phase a and the connected grid voltage are shown in Figure 3.9 below. Two periods are shown for clarity.
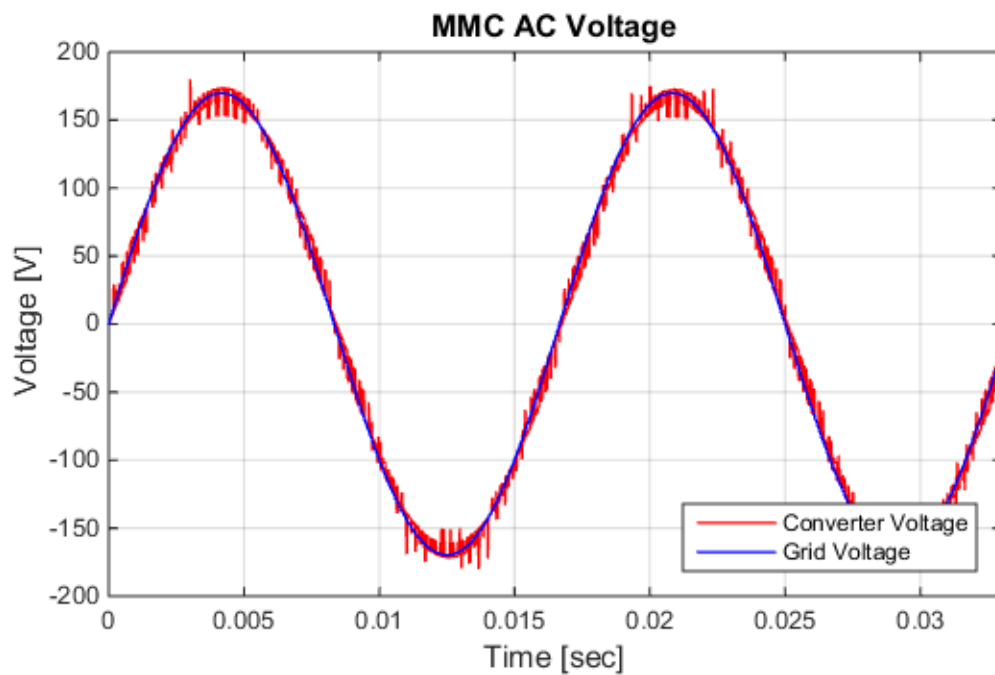

Figure 3.9 MMC AC-side voltages under PI control

3.2 PR CONTROL SIMULATION

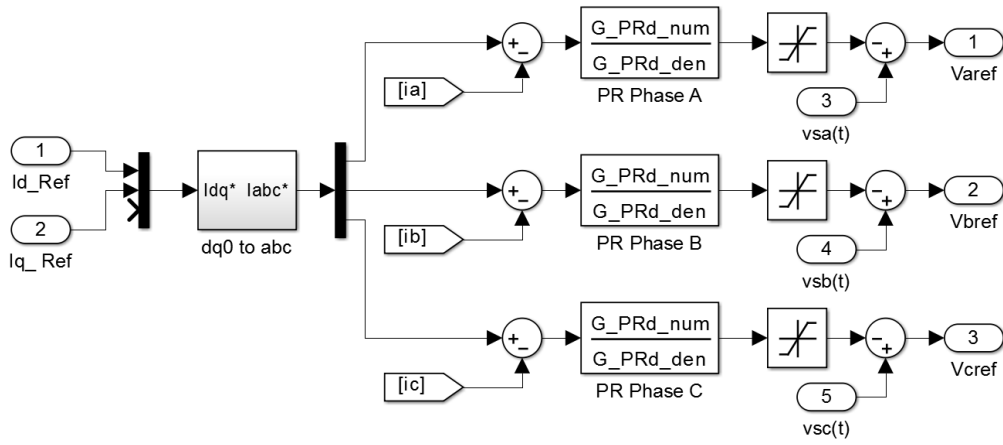The control scheme for the PR controller is shown below in Figure 3.10.

Figure 3.10 PR controller Simulink model

The blocks labeled 'PR Phase j' are the discrete versions of the continuous-time PR controller. The discrete transfer functions were derived by the c2d() function in MATLAB. The quantities labeled '[ij]' are the current measurements in each phase leg. Notice there is a separate controller needed for each phase when the current references are converted back to the natural frame.

The controller parameters are calculated using the method described in (33), where k_p is 0.676 and k_r is 298.456. The PR controller's step response to the manually generated reference is shown in Figure 3.11.
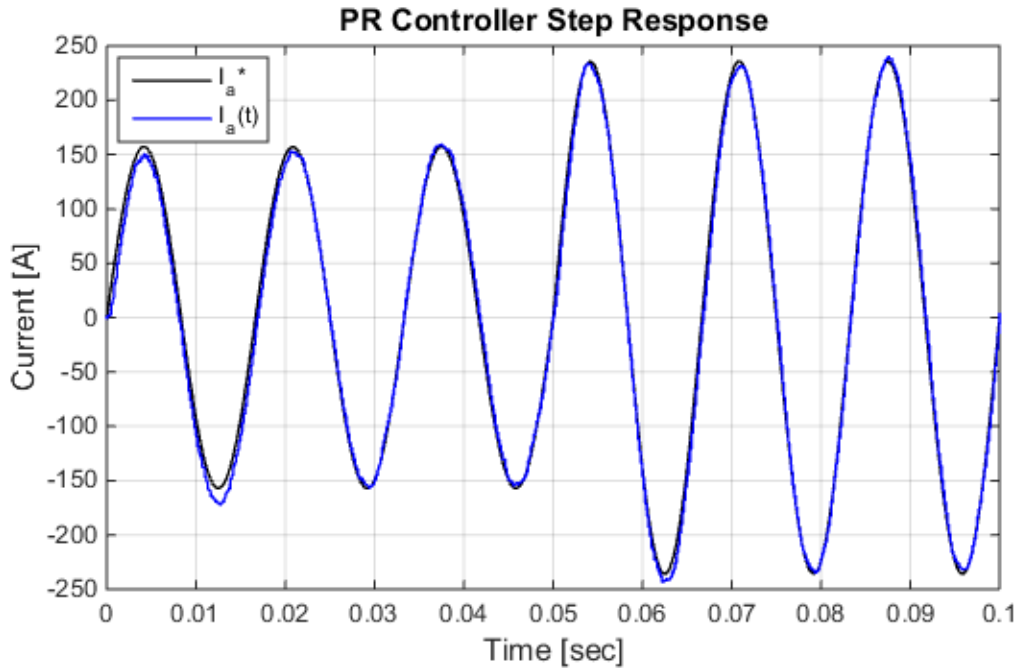
Figure 3.11 PR controller simulation step response

The controller tracks the step change in current well, due to the high gain at the fundamental frequency. Under normal operating conditions the reference current won't change instantaneously; the controller's bandwidth is within the stable operating range.

Just like with the PI controller, the PR controller version will now be tested with the addition of the outer power regulator. The power set point will be changed from 40 kW to 60 kW at 0.2 seconds. The AC and DC power transients are shown in Figure 3.12.
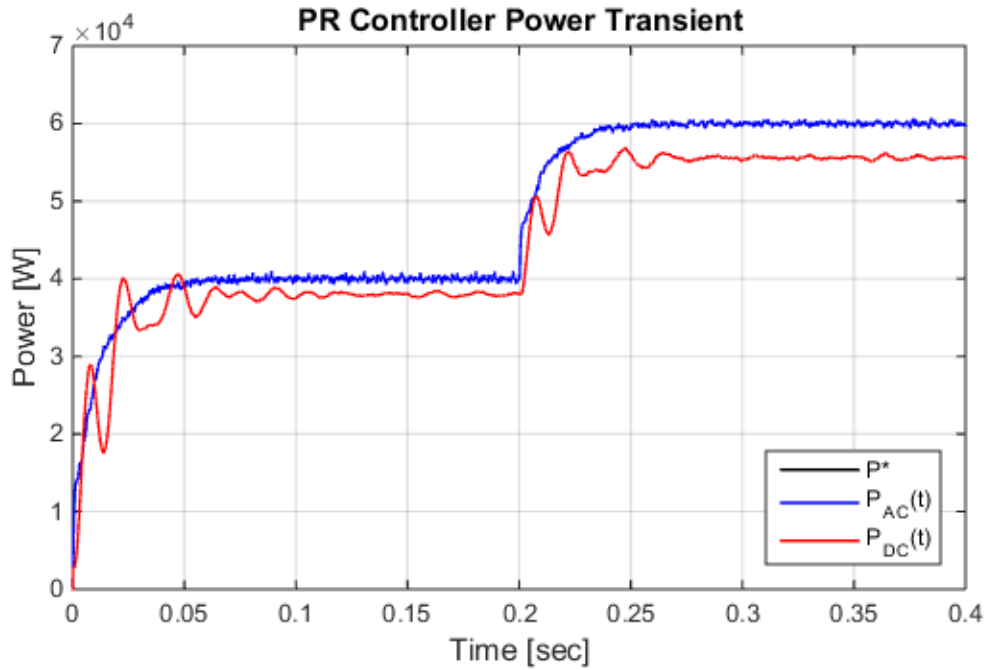
Figure 3.12 PR control AC and DC power transient

The transient dynamics are much better in comparison to the PI. The efficiency is identical to the PI version, at 95-92.5%. The current in phase a is shown in Figure 3.13.
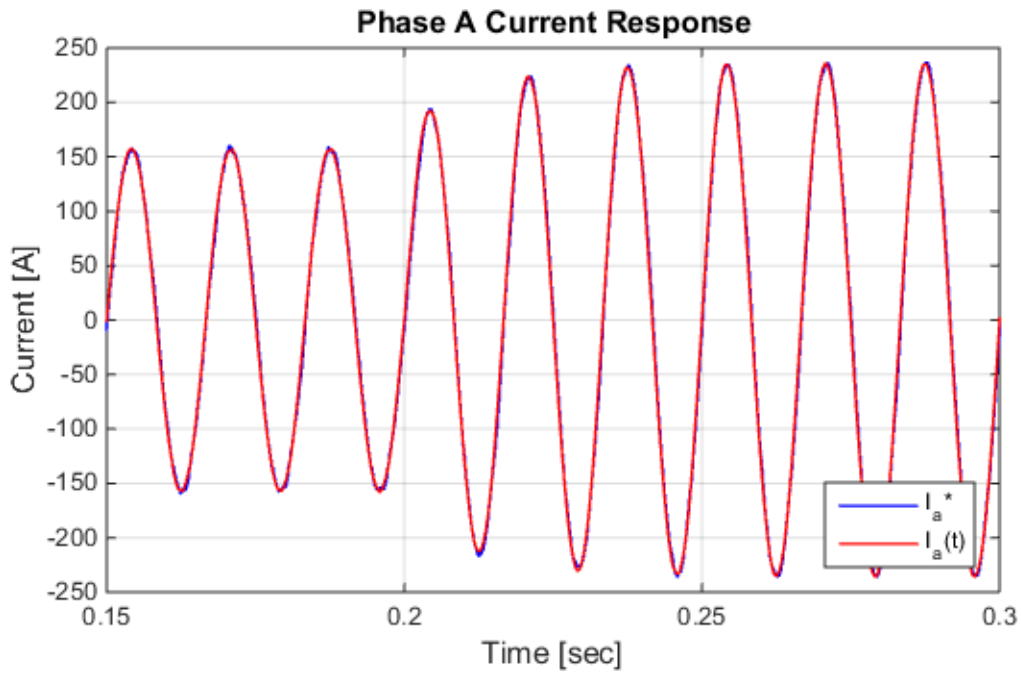

Figure 3.13 Phase a current tracking under PR control

Since the two controllers are operationally very similar, the system's overall response is close to that of the PI control in terms of tracking response in general.

The error signal $e_i(t)$ for the PR control implementation is shown in Figure 3.14. The error is similar in amplitude and frequency than that of the PI controller.
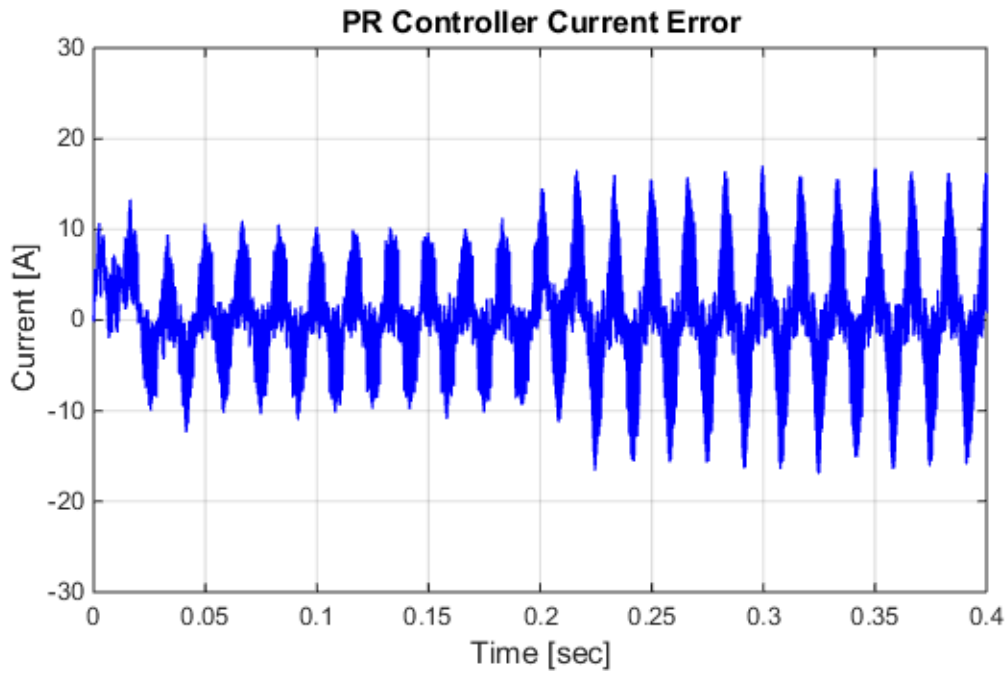

Figure 3.14 PR controller simulation error

As expected, the magnitude of the error is almost identical to the PI controller. There is noticeably less harmonic content in the error. The peak-to-peak error amplitude is the same as with the PI controller version, at 19 A and 28 A the current error is about 5.5-6% of the total phase current.

The circulating currents are also measured and plotted in Figure 3.15, and are expectedly similar to the PI controller results.
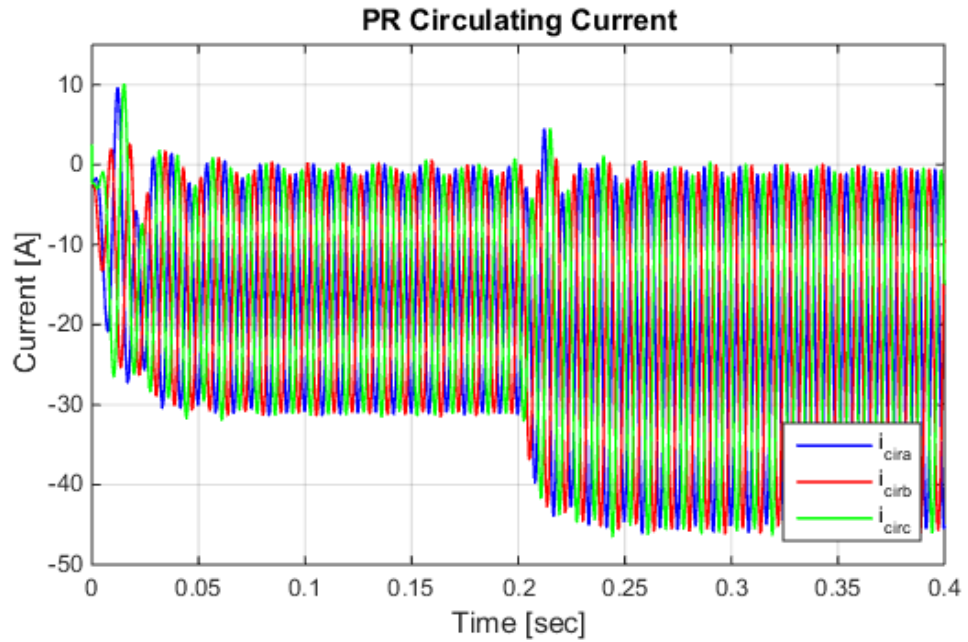
Figure 3.15 PR control circulating currents

The AC component magnitudes are nearly identical to the PI controller. The unwanted circulating currents present in the phases are approximately 9.5% of the total arm current. Figure 3.16 shows four periods of the circulating current in steady state.
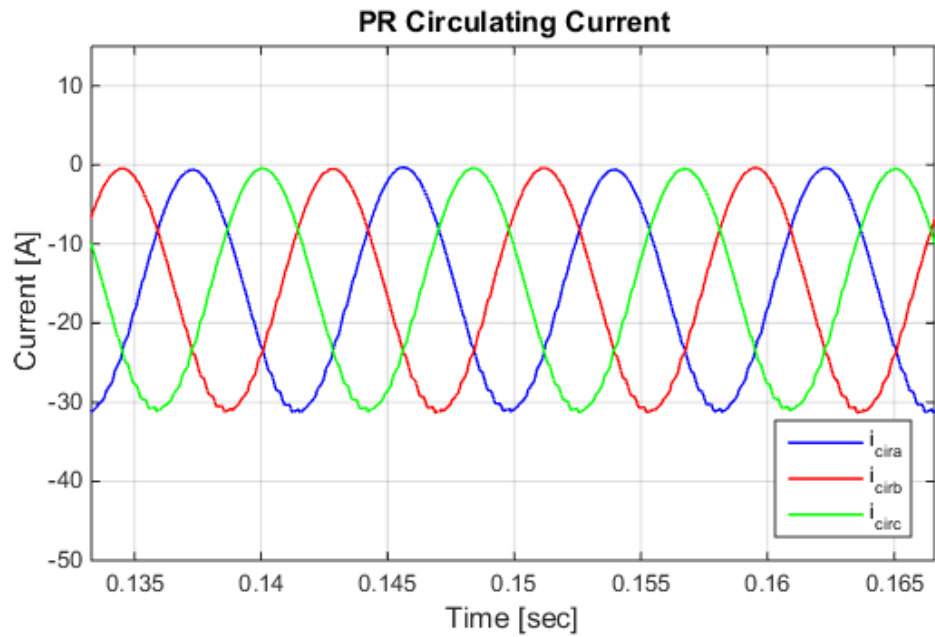

Figure 3.16 PR control circulating currents (zoomed)

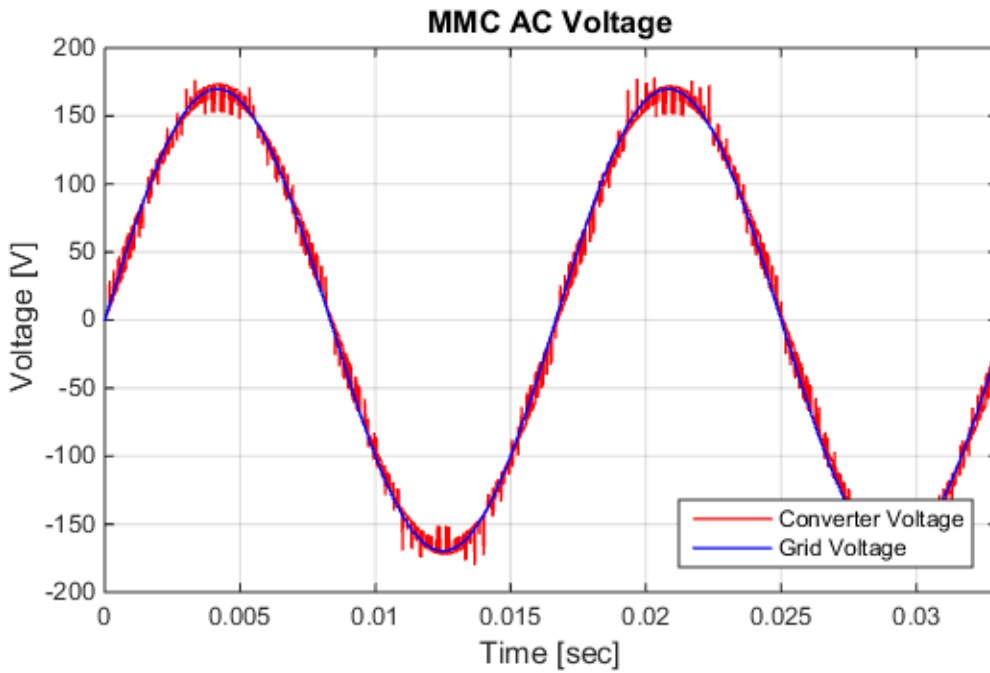The MMC output voltage for phase a is shown in Figure 3.17 below.

MMC AC Voltage

Figure 3.17 MMC AC-side voltages under PR control

3.3 PREDICTIVE CONTROL SIMULATION

The third current controller implementation is the predictive, or digital deadbeat, controller. The control scheme for this implementation is slightly more complex than that of the previous controllers. One main difference is that for this control approach, there are a total of six controllers needed because there is one for each of the converter's arms. The control schematic that includes both the positive and negative arm current controllers of phase a is shown below in Figure 3.18. It should be noted that the transmission line inductance L_c is assumed to be very small, such that the voltage drop across it is negligible. Each arm current controller is independent, but the two are shown together here because both control equations use the measured phase voltage, v_{sa}.
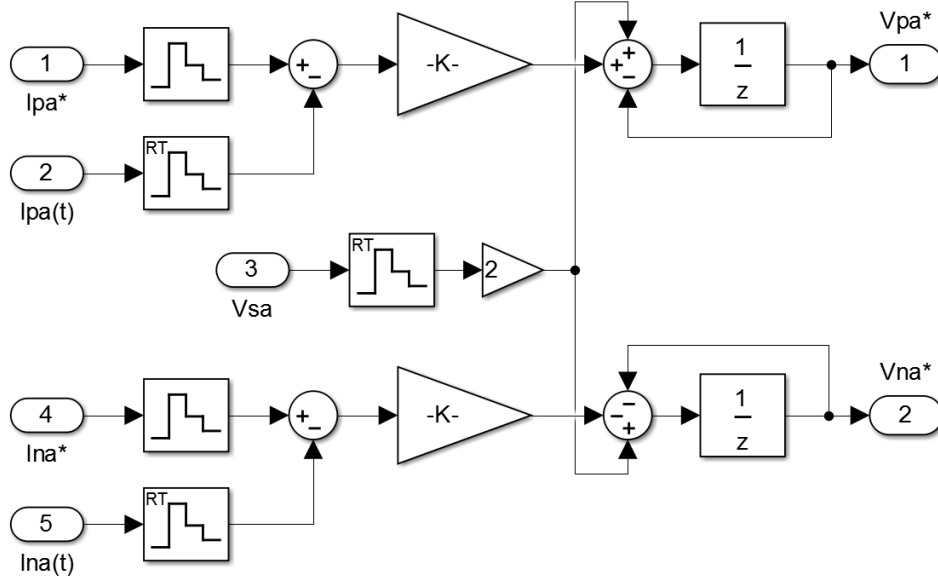
Figure 3.18 Phase a predictive Simulink model (-K- $= \dfrac{L_o}{T_{samp}}$)

The model shown above was built based on the control equations previously derived in (38) and (39), where 'p' and 'n' represent the positive and negative arm of phase j. The voltage references generated are then normalized and sent to the modulator.

In the PI and PR implementations, one current reference is generated for each phase leg. The problem with this approach is any current circulating between the arms of a phase leg is invisible to the current controller as long as the total phase current matches the reference. This predictive control approach requires a reference for each arm, or two separate references per phase leg, so the current reference generated by the power regulator is simply split according to (35) and (36), the DC current component $I_{dc}/3$ is calculated by (44), and the instantaneous power measurement $P(t)$ is shown in (45).

$$\frac{I_{dc}(t)}{3} = \frac{1}{3}\frac{P(t)}{V_{dc}(t)} \tag{44}$$

$$P(t) = v_a(t)i_a(t) + v_b(t)i_b(t) + v_c(t)i_c(t) \tag{45}$$

55

If the unwanted circulating current term i_{zj} is set to zero in both arm current equations, they become the ideal current reference equations for each converter arm. This approach inherently reduces the circulating currents present in the phases, as is shown in the following results.

The overall control scheme, including the reference current splitting mechanism is shown in Figure 3.19. Each of the 'Deadbeat Phase j' blocks contains both the positive and negative arm current controllers for the corresponding phase, which is exactly what was shown previously in Figure 3.16. The reference splitter block takes the three phase current references and outputs the six corresponding arm current references.
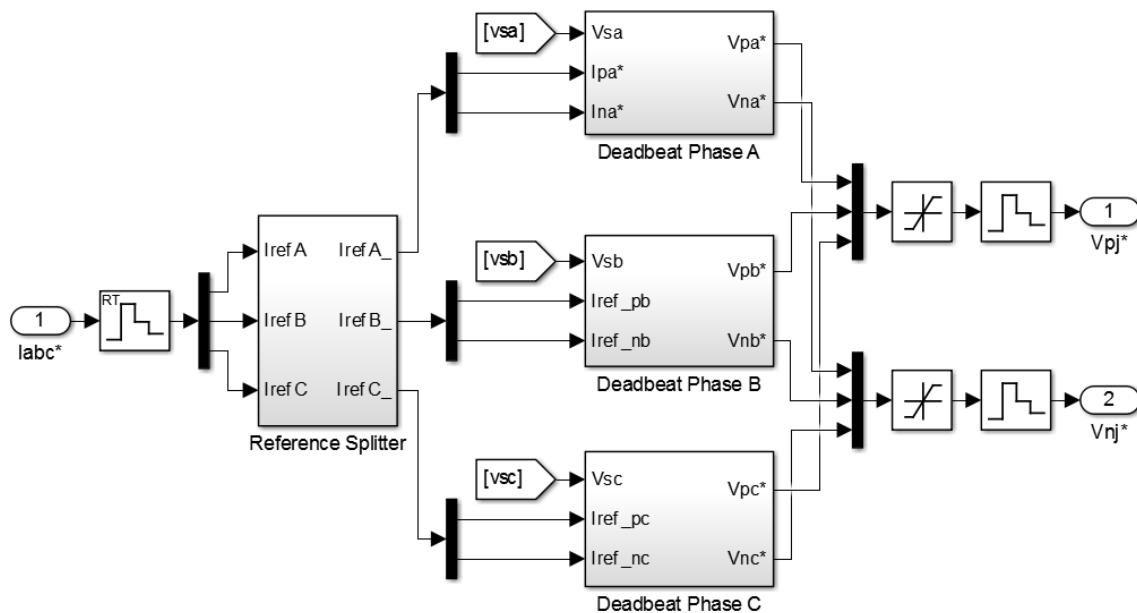

Figure 3.19 Predictive control Simulink model

The current reference 'Iabc*' is a 3x1 vector of the natural-frame phase current references generated by the power regulator. These references are sampled, and then split into the corresponding reference for each arm. The tags labeled 'vsa', 'vsb', and 'vsc' are the AC grid voltages connected to the MMC.

The first test case is again excluding the outer control loop and manually generating a current reference. The result for arm current I_{pa} is shown in Figure 3.20. The deadbeat controller reacts to the set point step change very quickly as expected, but there is a fairly significant tracking error present between the reference and the measured arm current. The source and mitigation strategy to reduce this will be discussed later.
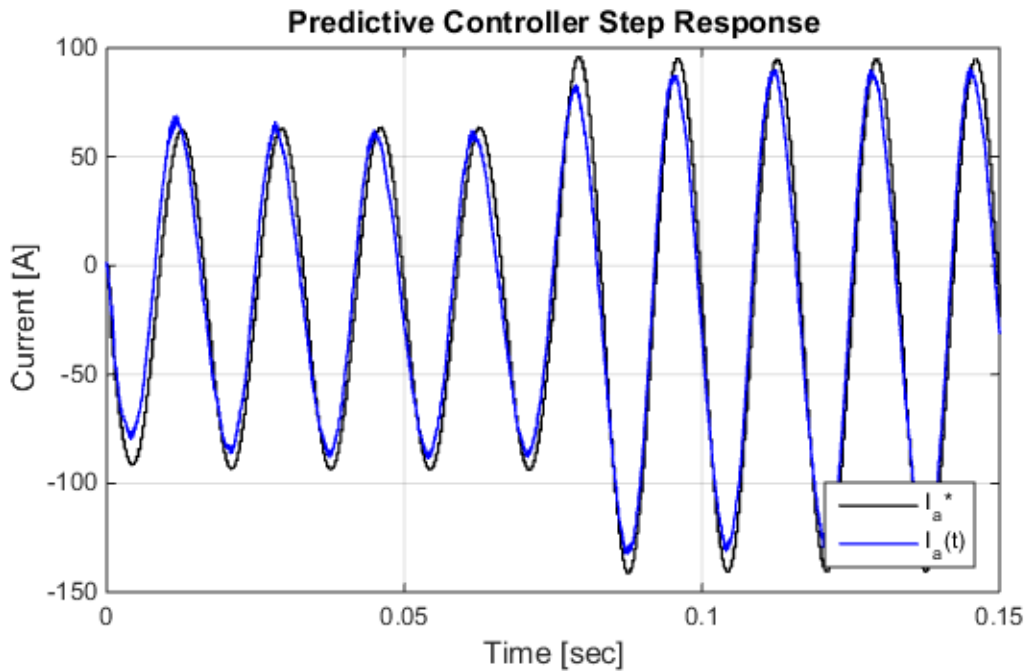

Figure 3.20 Predictive controller simulation step response

Just as with the previous two versions, the power regulation loop is included in the simulation and tested. The power transient results are shown in Figure 3.21.
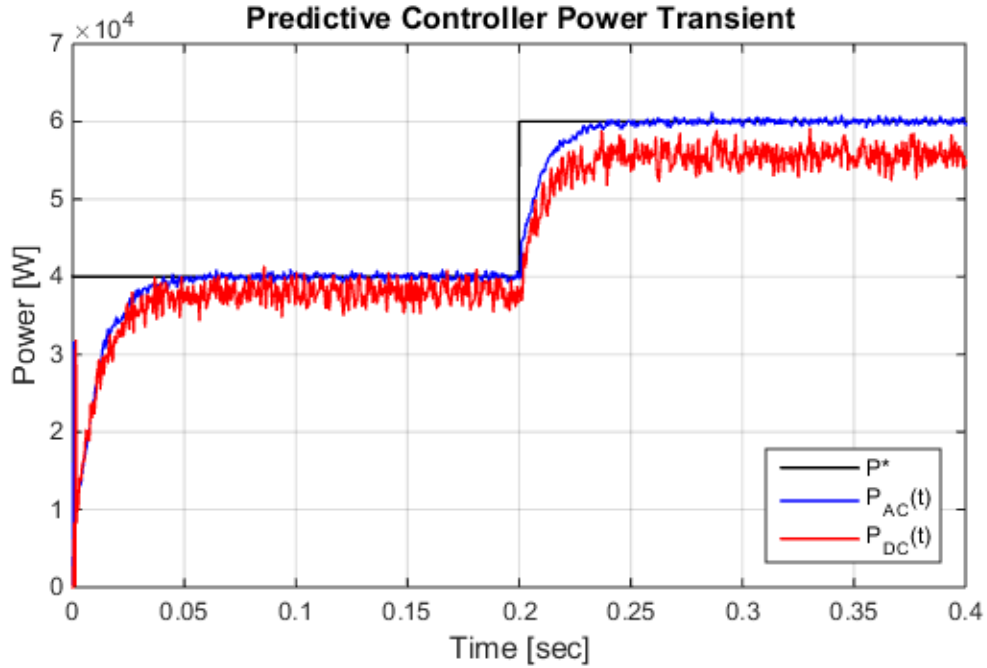
Figure 3.21 Predictive control AC and DC power transient

Aside from steady state error due to converter losses, the DC power tracks the AC power almost identically with no overshoot. The converter efficiency ranges from ≈92.5-95%.

There is, however, much more high frequency noise present in the DC current. Since the two arm currents are controlled independently in this implementation, the upper and lower arm capacitors are switched in and out of the circuit at different times in the same phase. This leads to variations in the arm current because of the properties of capacitor current in general, $i_C = C\frac{dv}{dt}$. Where, in previous implementations there were almost always six total submodule capacitors connected at any given time in each phase with voltage variations of ±13.3 V, now there may be instantaneous voltage variations of ±133.3-266.6 V as submodules are switched on and off independently. These high frequency current variations will also be visible in the circulating current waveforms.

The arm current response with the outer loop included is shown in Figure 3.22.
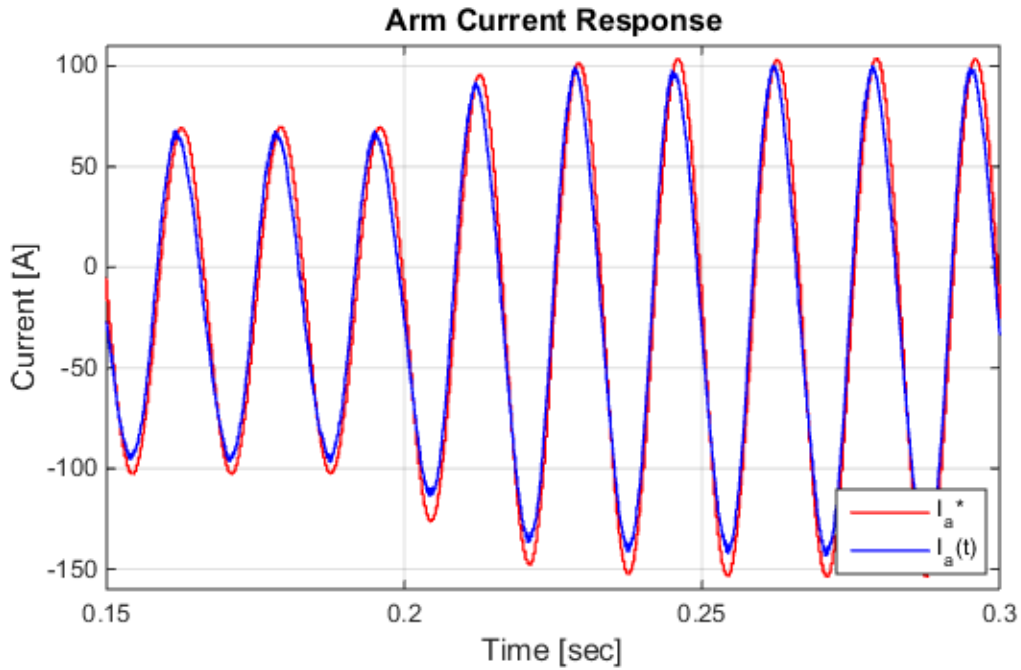
Figure 3.22 Arm current tracking under predictive control

Again, the tracking error is visible and constant; however, the deadbeat controller clearly

reacts to the step change very quickly. This error is quantified and plotted in Figure 3.23.
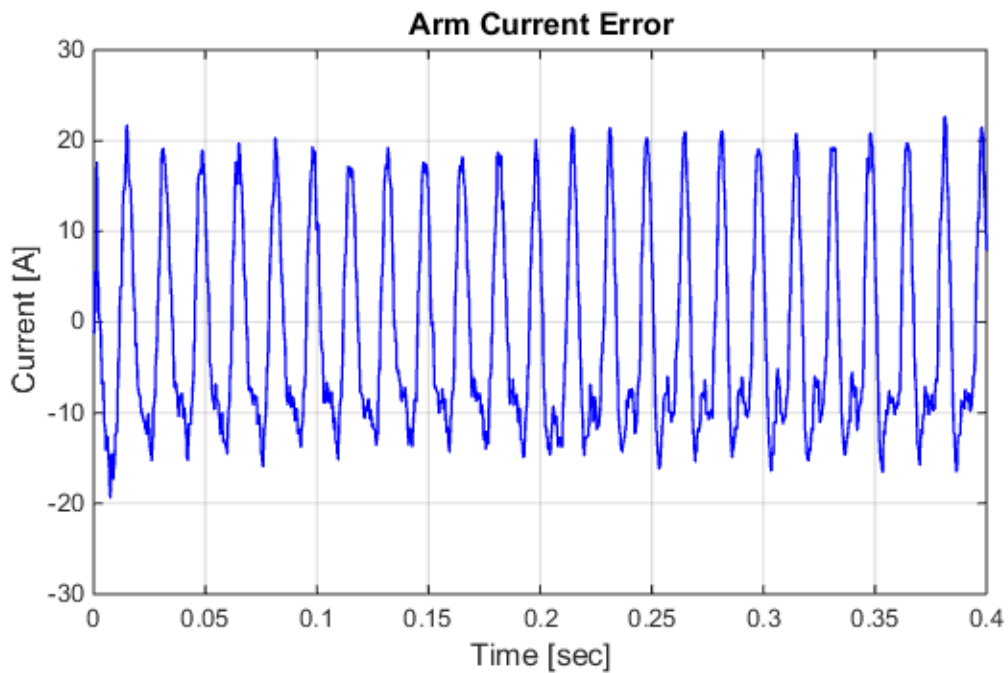

Figure 3.23 Predictive controller arm current error

The peak-to-peak current error for the deadbeat controller is shown to be around 30 A for both of the power set points.

The results presented so far have been of the performance of one of the six predictive controllers, specifically the positive arm current controller for phase a. Since this control approach requires a dedicated controller for each converter arm, it is necessary to look at the response of the entire phase a current in order to compare the result with the PI and PR implementations.

The phase a current response to the active power step change from 40 kW to 60 kW is shown in Figure 3.24. The waveform has been captured around the step time of 0.2 to better show the dynamics.
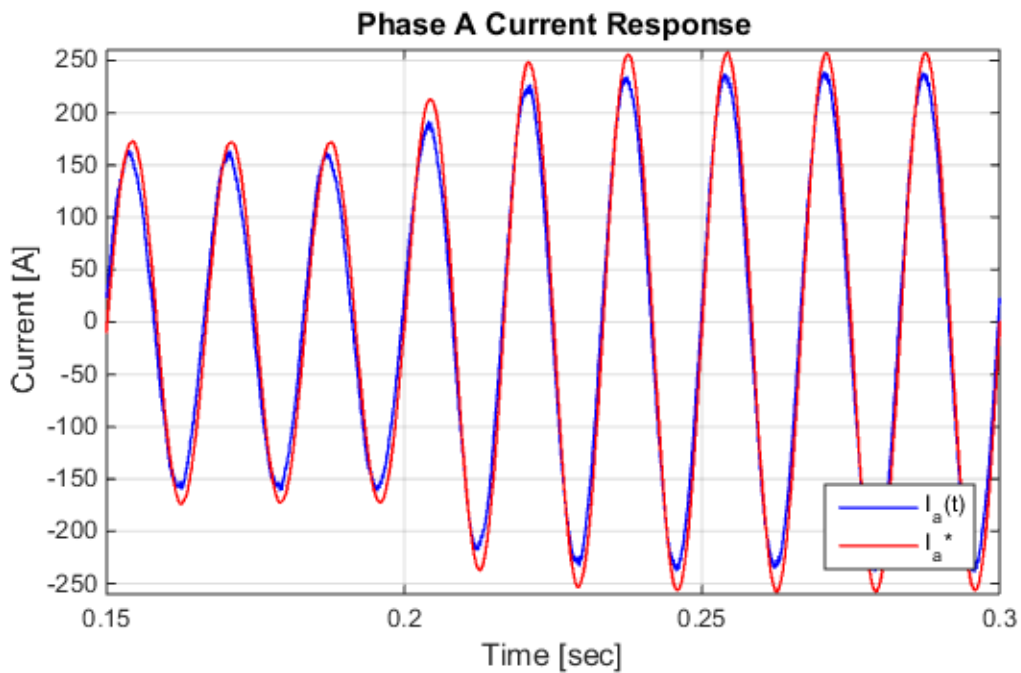

Figure 3.24 Phase a current tracking under predictive control

The system under deadbeat current control tracks the reference current change very well; however, a steady state error is present at the peaks of the waveform.

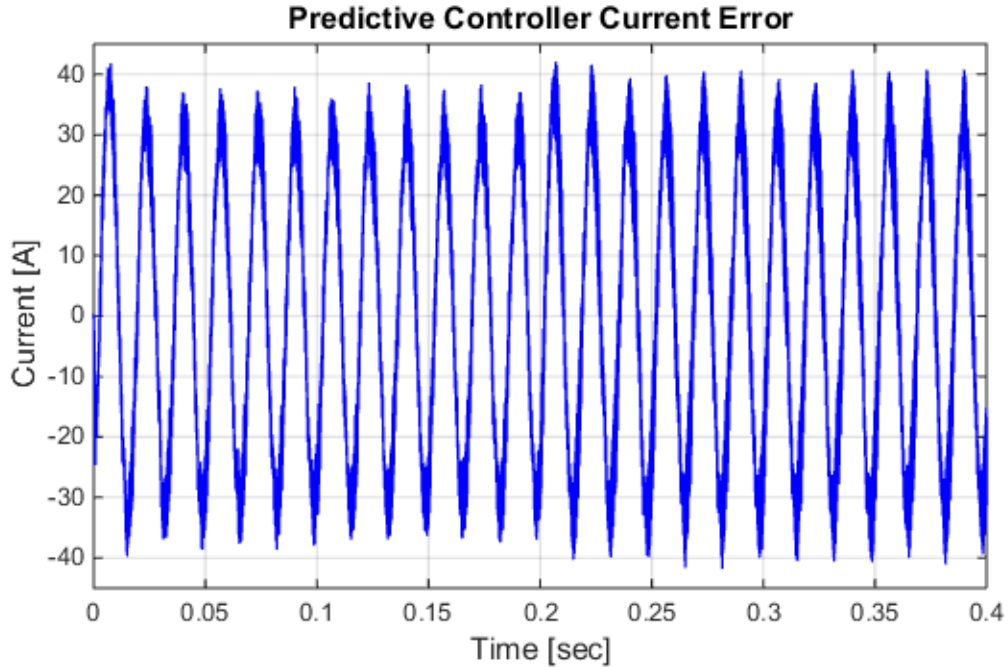The error in this waveform has been quantified and shown in Figure 3.25.

Figure 3.25 Predictive controller simulation phase current error

The error magnitude ranges from approximately 66 A to 72 A, which is significantly larger in comparison to both the PI and PR controller implementations, at approximately 15-20% of the entire arm current in comparison to 6.3% in the PI and PR versions.

The tracking error visible at the phase current peaks is due to the assumption that the two DC bus terminals of V_{dc}^+ and $-V_{dc}^-$ with respect to ground are known and constant at $400\ V$ and $-400\ V$, respectively. During converter operation, however, the magnitude of the bus voltages varies slightly as each arm's submodule capacitors are inserted and bypassed at different times and for different durations throughout the simulation. The measurement of the positive and negative terminals to ground (V_{pdc-g} and V_{ndc-g}) is shown in a schematic in Appendix Figure A.2. The measurement of both taken in simulation is shown in Figure 3.26.
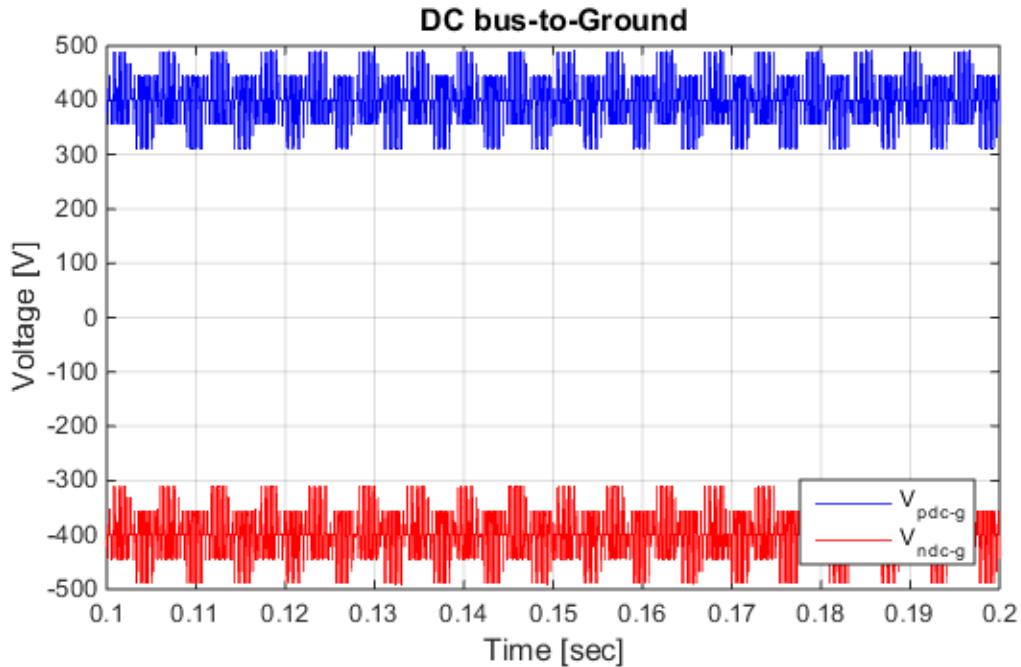
Figure 3.26 Positive DC-bus to ground variation

The peak variation from the nominal (-)400 V is approximately $\pm 90\,V$, however the value is changes very rapidly due to the PSC-PWM method that has three reference signals which cause the submodules to change state three times per sample period.

An interesting view of the V_{pdc-g} measurement superimposed onto the plot of the current error in all three phases is shown in Figure 3.27. Note that the axes are labeled for the current error measurement, not voltage. The V_{pdc-g} measurement is shown in gray and normalized around 0 A to show its relationship to the current error over time.

62

Figure 3.27 Zoomed in phase current error vs. V_{dc}^+ measurement

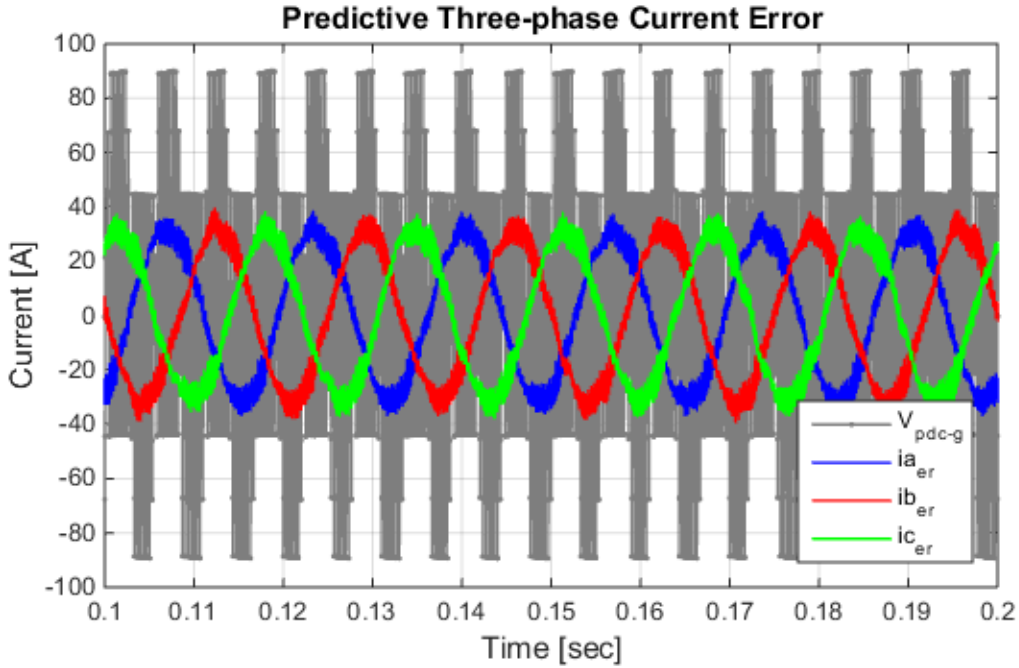As shown, the maximum error in each phase directly correlates to the largest variations in the DC-bus terminals.

The predictive control algorithm indirectly determines the number and the duration of submodule connections and disconnections by computing the average value of the controlled voltage source V_{pj} for the next sample $(k + 1)$ that will yield the desired arm current for that control interval. In order to produce the average voltage value requested by the controller, the modulator switches the appropriate number of submodules into and out of the circuit. This means that the predictive controller's output is directly related to the DC-bus variation. One way to compensate for this error would be to incorporate a prediction for the DC-bus voltage variation at sample (k+1) based on the predictive controller's computed value for $V_{pj}(k + 1)$ and $V_{nj}(k + 1)$. While this would

be an interesting addition to the control implementation, it is outside the scope of this study.

The main objective of this comparison is to verify the circulating current reduction of this novel predictive control approach. The circulating current measurement is shown in Figure 3.28.
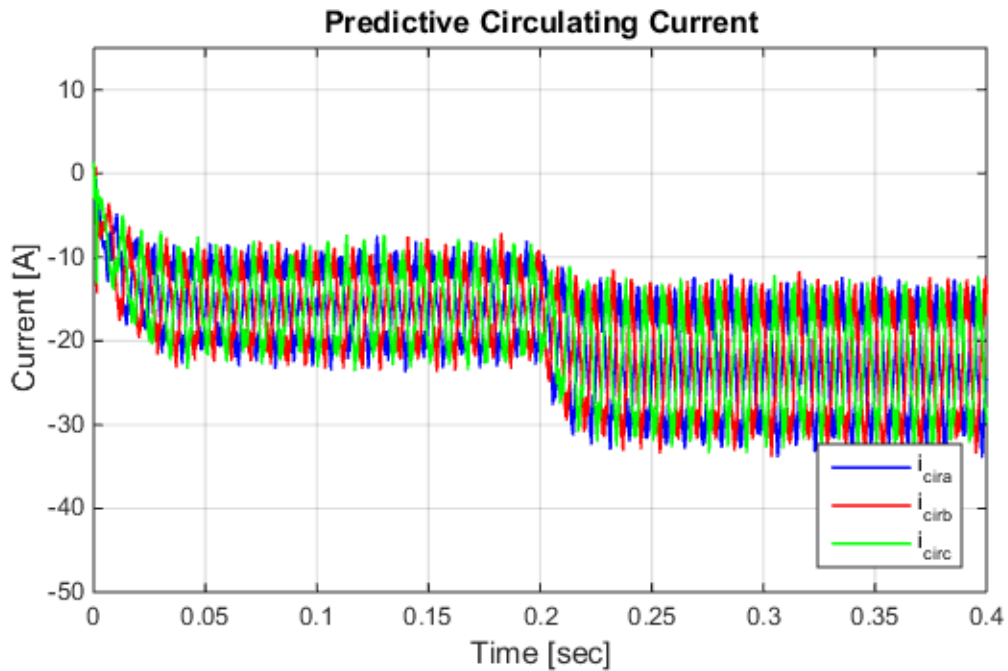
Figure 3.28 Predictive control circulating currents

The peak-to-peak magnitude of the circulating currents is approximately 11 A and 16 A at 40 and 60 kW, which is significantly reduced in comparison to both the PI and PR implementations. The circulating current magnitude is approximately 3.5% of the total phase current, which is a 63% reduction of total circulating current magnitude from the PI and PR implementations. This improvement is the result of the individual arm currents being directly controlled by a dedicated reference signal and controller so that any unwanted current components are reduced. The remaining circulating current that appears

is attributed to both the incomplete DC-bus to ground prediction made in the control design and the efficacy of the capacitor voltage balancing technique.

The high frequency content present in the power output in Figure 3.19 previously can be attributed to the circulating current harmonic content. Four periods of the circulating currents are shown in Figure 3.29.
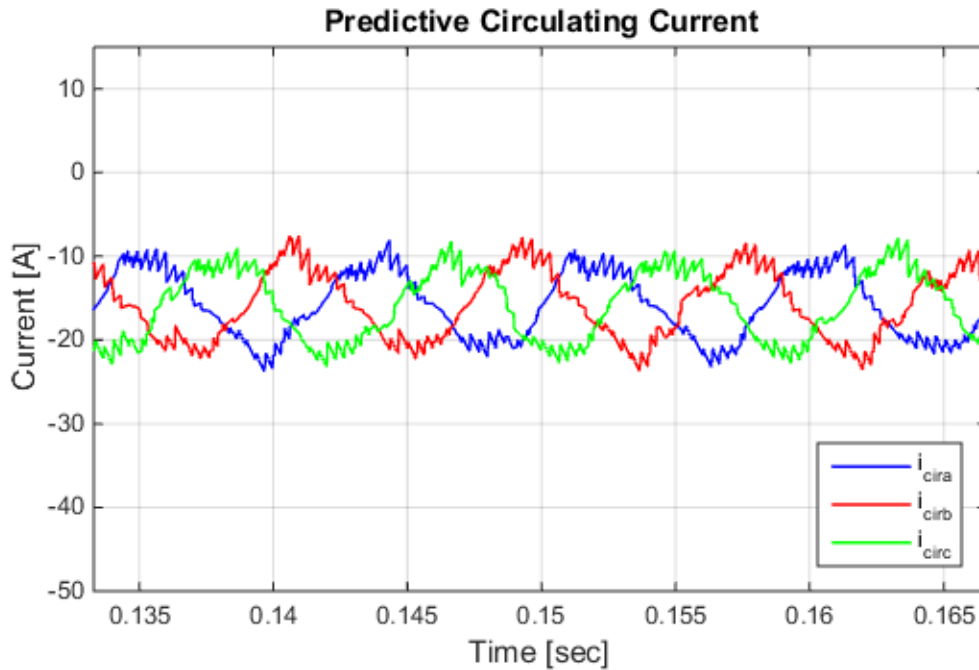

Figure 3.29 Predictive control circulating currents (zoomed)

Lastly, the MMC output voltage for phase a is shown in Figure 3.30 below. The converter's output matches the grid voltage very well, and there is no visible phase shift.
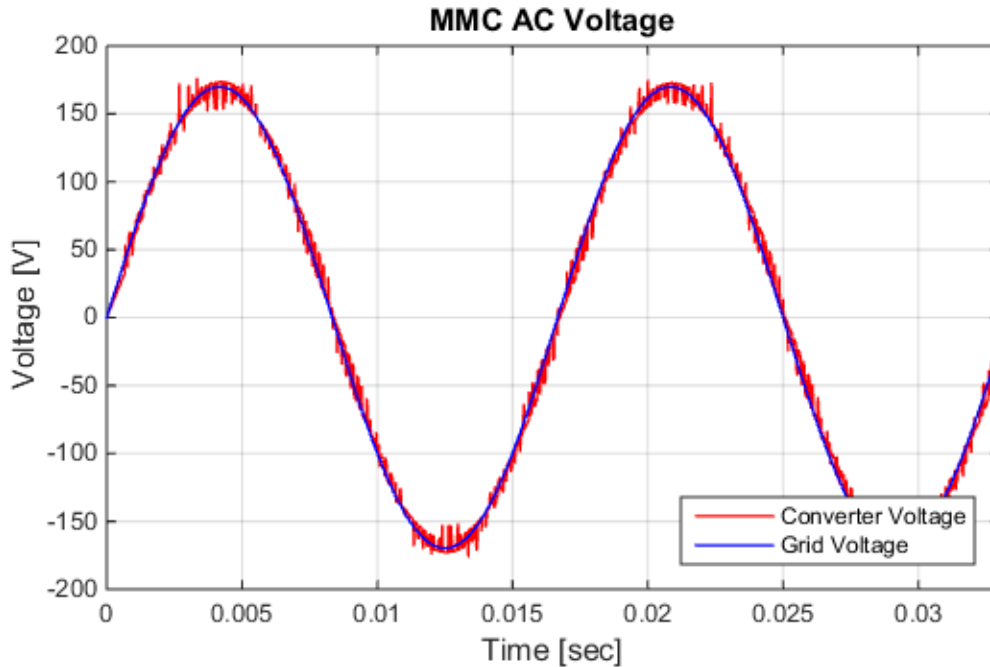
Figure 3.30 MMC AC-side voltages under predictive control

3.4 TOTAL HARMONIC DISTORTION

Because modular multilevel converters are normally connected to a utility grid, the converter output voltage harmonics could cause grid voltage distortion. One of the main benefits of the MMC topology is the inherent reduction of harmonics due to the small incremental changes in output voltage in comparison to conventional VSCs. The total harmonic distortion (THD) measurement is a way of quantifying the voltage distortion of a waveform by calculating the ratio of the sum of all harmonic component power to the power of the fundamental frequency. This measurement was taken for 20 cycles at steady state of the output waveform under each method of current control. The results are shown in Table 3.2.

Table 3.2 THD Measurements

Control Method	THD (%)
Proportional Integral (PI)	5.58
Proportional Resonant (PR)	5.51
Predictive (Deadbeat)	4.88

Since the converter has the same modulation and capacitor voltage balancing techniques,

the THD is shown to be very similar for all three current control techniques, as expected.

CHAPTER 4

CONCLUSION

The intent of this research was to investigate different current control strategies for a modular multilevel converter and compare the performances of each. Specifically, a novel approach to predictive control of an MMC with inherent circulating current reduction was presented and compared to the more conventional strategies of synchronous proportional-integral and resonant control. To accomplish this goal, a MMC model was developed using MATLAB and Simulink and a cascaded control scheme was created to control its operation. From these results, the predictive control approach presented in this paper is validated as a viable method for current control of an MMC, and its inherent benefit of reduced circulating current is established.

The design method for each control approach was presented and then individually validated with simulation results. Then, each control approach was included in the cascade control loop and the converter's efficiency, phase current error, and circulating current magnitude were analyzed and compared. The PI and PR controllers had similar results, while the predictive controller had about three times as much phase current error in comparison. The predictive controller also had a 63% reduction in circulating current compared to the PI and PR models. The circulating current ultimately distorts the sinusoidal arm currents and leads to increased converter losses, so the reduction of these currents is clearly an advantage for this control type. Finally, the total harmonic distortion

of the MMC's output voltage was quantified under each current control method and the predictive controller showed a slight decrease in THD in comparison to the PI and PR implementations.

REFERENCES

[1] A. Lesnicar and R. Marquardt, "An Innovative Modular Multilevel Converter Topology Suitable for a Wide Power Range," *IEEE Bologna PowerTech Conference,* pp. 1-6, 2003.

[2] S. Rohner, S. Bernet, M. Hiller, and R. Sommer, "Modelling, simulation and analysis of a modular multilevel converter for medium voltage applications," in *Proc. IEEE Int.Conf. Ind. Technol.*, Vina del Mar, Chile, 2010, pp. 775-782.

[3] A. Lesnicar, "Neuartiger, modularer mehrpunktumrichter M2C für netzkupplungsanwendungen," Ph.D. dissertation, Dept. Elect. Eng. Inf. Technol., Univ. of Bundeswehr, Munich, Germany, 2008.

[4] Q. Tu, Z. Xu, H. Huang, and J. Zhang, "Parameter design principle of the arm inductor in modular multilevel converter based HVDC," in *Proc. Int. Conf. Power Syst. Technol.*, Hangzhou, China, 2010, pp. 1–6.

[5] Prawin Ange, Michael and Dr. N. Devarajan, "SVPWM Pattern Generation using Field Programmable Gate Array Implementation," *IPCSIT,* vol. 3, pp. 435-439, 2011.

[6] R. Blackmon, "Analysis of Modulation and Voltage Balancing Strategies for Modular Multilevel Converters," M.S. Thesis, Dept. Elect. Engr., Univ. S. Carolina, Columbia, 2013.

[7] S. Buso and P. Mattavelli, *Digital Control in Power Electronics*. San Rafael, CA: Morgan & Claypool, 2006.

[8] Q. Tu, Z. Xu and L. Xu, "Reduced Switching-Frequency Modulation and Circulating Current Suppression for Modular Multilevel Converters," *IEEE Transactions on Power Delivery,* vol. 26, pp. 1-9, 2011.

[9] P. Munch, D. Gorges, M. Izak, and S. Liu, "Integrated current control, energy control and energy balancing of modular multilevel converters," in *Proc. IEEE 36th Annu. Conf. Ind. Electron. Soc.*, 2010, pp. 150-155.

[10] Yan Ma and Lingling Fan, "Integrated control and switching strategy for a grid-connected modular multilevel converter," in *Power & Energy Soc. Gen. Meeting., IEEE*, pp.1-5, 26-30 July 2015

70

[11] Middlebrook, R.D., "Topics in Multiple-Loop Regulators and Current-Mode Programming," in *Power Electron., IEEE Transactions*, vol.PE-2, no.2, pp.109-124, April 1987.

[12] N. Mendalek and K. Al-Haddad, "Modeling and nonlinear control of shunt active power filter in the synchronous reference frame," *Harmonics and Quality of Power, Proc. 9th Int. Conf.*, vol. 1, pp. 30-35, 2000.

[13] M. Hagiwara and H. Akagi, "Control and Experiment of Pulsewidth-Modulated Modular Multilevel Converters," *IEEE Transactions on Power Electron.,* vol. 24, pp. 1737-1746, 2009.

[14] Hu Pengfei; Jiang Daozhuo; Zhou Yuebin; Guo Jie; Lin Zhiyong, "Study of the Proportional Resonant Control Based Modular Multilevel Converter," in *Digital Manuf. and Automation (ICDMA), 3rd Int. Con.*, pp.810-813, July 31-Aug. 2 2012.

[15] N. Zhang, H. Tang, and C. Yao, "A Systematic Method for Designing a PR Controller and Active Damping of the LCL Filter for Single-Phase Grid-Connected PV Inverters," in *Energies*, vol.7, no.6, pp.3934-3954, June 2014.

[16] Dumitrescu, A.M.; Griva, G.; Bojoi, R.; Bostan, V.; Magureanu, R., "Design of current controllers for active power filters using naslin polynomial technique," in *Power Electron. and Applic., European Conference*, pp.1-7, 2-5 Sept. 2007.

[17] Jiangchao Qin; Saeedifard, M., "Predictive control of a three-phase DC-AC Modular Multilevel Converter," in *Energy Conversion Congress and Exposition (ECCE), IEEE*, pp.3500-3505, 15-20 Sept. 2012.

[18] S. Bacca, I. Munteanu and A. I. Bratcu, "Naslin Polynomial Method," in *Power Electronic Converters Modeling and Control*, London, England: Springer-Verlag, 2014, ch. 9,sec. 9.3.3.3, pp. 257-261.
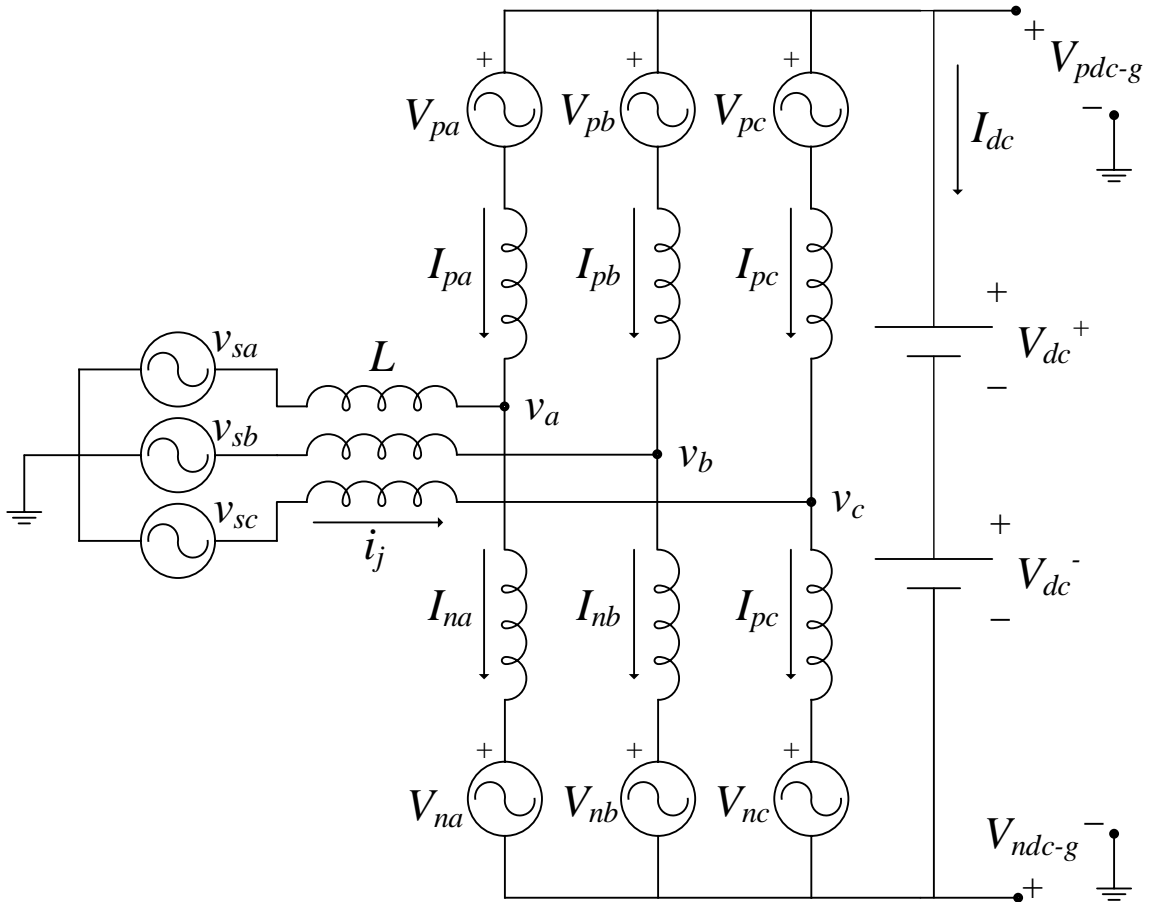
APPENDIX A – MEASUREMENT SCHEMATIC

Figure A.1 DC-bus voltage variation measurement locations